TOWARDS ROTATIONAL CONTROL OF MOLECULES IN HELIUM NANODROPLETS

by

Jordan A. M. Fordyce

B.Sc., University of Alberta, 2015

A THESIS SUBMITTED IN PARTIAL FULFILLMENT
OF THE REQUIREMENTS FOR THE DEGREE OF

Master of Science

in

THE FACULTY OF GRADUATE AND POSTDOCTORAL STUDIES
(Physics)

The University of British Columbia
(Vancouver)

June 2020

The following individuals certify that they have read, and recommend to the Faculty of Graduate and Postdoctoral Studies for acceptance, the thesis entitled:

TOWARDS ROTATIONAL CONTROL OF MOLECULES IN HELIUM NANODROPLETS

submitted by **Jordan A. M. Fordyce** in partial fulfillment of the requirements for the degree of **Master of Science** in **Physics**.

Examining Committee:

Dr. Valery Milner, Physics
Supervisor

Dr. Takamasa Momose, Chemistry
Supervisory Committee Member

Abstract

The feasibility of using rotating molecules as "nanoprobes" for testing the superfluidity of helium nanodroplets is explored in this thesis. Helium nanodroplets have an internal temperature of 0.37 K and are below the superfluid transition temperature in bulk helium of 2.17 K. The onset of superfluidity in this microscopic environment will be explored by rotationally exciting molecules using a tool called an optical centrifuge. This tool affords a high degree of precision in the final rotational frequency that the molecule will reach and makes it useful in probing the coupling between the rotor and helium. A unique helium nanodroplet vacuum chamber system was characterized for the range of operation possible, especially with focus on the signal to background detection conditions. Two techniques were explored to characterize the dynamical rotational behaviour of the molecules in these conditions: direct measurement of the molecular orientation and direct measurement of the angular momentum state. The molecular orientation of a molecule is characterized by it's confinement to the rotational plane using $\langle \cos^2 \theta_{2D} \rangle$ as the metric. A $\langle \cos^2 \theta_{2D} \rangle$ measurement of ≈ 0.7 was successfully recovered from background for carbon disulfide doped helium droplets using an alignment probe pulse, however, with the centrifuge it was ultimately unclear if the molecule was rotating or simply aligning to the plane of rotation. The angular momenta of a molecule was characterized via its ion signal from a Resonance Enhanced Multiphoton Ionization (REMPI) scheme. The feasibility of measuring a transition in oxygen at the low signal to background densities was studied and would be promising to use with oxygen doped helium droplets. In order to continue the research, improvements need to be made to the set up and the two techniques should be used in tandem so that rotation can be better detected and characterized.

Lay Summary

Helium is a substance that is known to have superfluid properties at very low temperatures which means that it behaves like a fluid that creates no resistance or friction to objects moving through it. Helium nanodroplets are small clusters of helium atoms (1000 - 10000) that are created in a vacuum chamber. The ultimate goal is to investigate the superfluid properties of these nanodroplets using controlled rotation of a molecule. Using a special tool in our lab called an optical centrifuge, individual molecules that are placed inside of the helium nanodroplets can be set to rotate at frequencies up to 10 THz and be precisely controlled at the frequencies leading up to this limit. This work details the characterization of the apparatus used to create the helium nanodroplets and the preliminary work on two different techniques that can be used to study the rotation in this environment.

Preface

This thesis is based on the characterization of the helium nanodroplet apparatus and data taken for the optical centrifuge experiments that I conducted. The content of this thesis is not taken directly from previously published or collaborative articles.

Chapter 3 is a description of modifications and characterization performed primarily by me on the vacuum chamber system used to create helium nanodroplets that was designed and built by previous students. Chapter 4 includes calibration and detection imaging techniques that I learned from other groups subsequently implemented on our unique set up. Chapter 5 includes Monte Carlo simulations that I created to understand the signal to background conditions and the measurements I made that support the main lessons learned throughout the thesis.

Ian MacPhail-Bartley contributed a lot of the data acquisition software used to collect the data and he helped make the modifications necessary on the helium droplet machine to keep it working properly. A visiting student, Audrey Scognamiglio, was directly involved in the REMPI detection technique discussed in Chapter 4 and 5. She analyzed the spectra to assign the rotational states and was directly involved in collecting the data. Dr. Frank Stienkemeier was a collaborating partner involved in characterizing the helium nanodroplet apparatus discussed in Chapter 3. Dr. Alexander Milner was always available to help with the equipment, analysis, and for general discussions regarding any part of the project.

Dr. Valery Milner supervised the overall project, was always available to offer help, and assisted with editing the thesis.

Table of Contents

List of Tables

List of Figures

Glossary

CE Coulomb energy

CF optical centrifuge

FWHM full with half max

RE rotational energy

REMPI resonance enhanced multiphoton ionization

S:B signal to background

SMI spatial map imaging

TE total energy

VMI velocity map imaging

Acknowledgments

I would like to express my gratitude to my supervisor Dr. Valery Milner for supervising and supporting my research. I learned a great deal from my time in his lab and the project would not have progressed to the stage it did without his guidance. I would like to thank Dr. Alexander Milner for sharing his lab space with me, instilling his good lab habits in me, and for always being open to physics discussions. I would also like to thank Dr. Frank Stienkemeier for welcoming me to his lab in Freiburg and helping me gain confidence as a scientist - your support and wisdom was invaluable.

I am extremely grateful to have been able to work with everyone that was a part of the lab, but especially Ian MacPhail-Bartley, Walter Wasserman, and Audrey Scognamiglio. Your daily contributions made all of my work possible and you helped keep morale in the lab high. I look forward to seeing the scientists you become at the end of your projects! Audrey, in addition to the science you also helped me through so many tough moments. Thank you for being so consistently dependable and going for all of the coffee and cigarette breaks I needed.

I would also like to thank all my Van City ”frandz” who are probably only going to read the Acknowledgements part of my thesis to make sure they are referenced - you know who you are. I appreciate the support you’ve given me and you’ve made my time in Vancouver truly enjoyable.

Finally, I would like to thank my family for their constant support and encouragement. You made me the type of person who could conquer all of those late night

lab shifts and keep moving forward no matter what challenge was thrown my way. I would especially like to thank my mom, Sherry, who I lost along the way but was the first to introduce me to math and nurture my creativity.

Chapter 1

Introduction

Helium nanodroplets have been an exciting area of research since their introduction in 1992 [43]. They have been used for cryogenic matrix isolation in spectroscopy and as a reactor to synthesize new molecular complexes [25][45]. Studying the properties of individual nanodroplets is interesting and challenging as well. The discovery of superfluids and Bose-Einstein condensates demonstrate that a single quantum state can extend it's properties across macroscopic lengths, for example bulk ^{4}He has zero viscosity below the liquid phase transition temperature of 2.17 K [1]. While superfluidity in bulk medium is well understood, the onset of superfluidity in finite, microscopic systems such as clusters and helium nanodroplets is an active area of research. One of the first interesting findings was in the infrared (IR) absorption spectrum of SF_6 where the rotational lines were sharp and could be fit assuming a free molecular spectrum [15]. However, the line spacing revealed that the moment of inertia was larger by a factor of 2.8 from a free molecule and was hypothesized to be due to interactions between the molecule and the liquid helium environment. A follow up study was done to further test the superfluid nature of the helium nanodroplets and was called a microscopic Andronikashvili experiment, by embedding OCS inside of ^{4}He and ^{3}He nanodroplets [17]. ^{4}He nanodroplets have an internal temperature of 0.37 K and are in the superfluid regime but ^{3}He nanodroplets have an internal temperature of 0.15 K and are well above their superfluid transitional temperature of 3 mK. This allowed the IR spectrum of OCS to be observed in a normal fluid and in a superfluid while both were still cold,

microscopic environments. The study showed that OCS could freely rotate in ^{4}He but not in ^{3}He because the lines were sharp for ^{4}He and pronounced but a large, broad peak was seen for ^{3}He. However, the spacing was, again, different from a free molecule by about a factor of 3. This increased moment of inertia suggested that there could be local non-superfluid layers still existing [28] and that it depended on the anisotropy of the molecule.

Recently, understanding this polyatomic impurity problem with the quasiparticle approach typical in condensed matter physics has been employed and has been having success [30][10][40]. A quasiparticle describes microscopic interactions in a complicated environment as if they were the interaction between different particles. This approach introduces an "angulon" which describes the molecular rotor dressed by phonon interactions from the helium nanodroplets. This is done to simplify the computational demand that would be required to consider all the degrees of freedom in the problem. The scaling of the moment of inertia seen in the previously mentioned experiments, or "renormalization" of the rotational constant, can be explained from the strength of the interaction between the molecule and the helium bath [29]. In the strong coupling limit, generally describing heavy rotors where the interactions with the helium atoms happen to be strong, a nonsuperfluid helium shell rotates along with a slowly moving molecule. This regime predicts a decrease in the rotational constant on the order of a factor of 3 for molecules like OCS, SF_6, or CS_2 as expected from experiment. In the weak coupling limit, generally describing the light rotors, renormalization occurs due to a slightly different process and the rotational levels are shifted due to virtual phonon absorption. This regime predicts less of a decrease in the rotational constant, and rotors like C_2H_2 are barely shifted from their free molecule rotational constant.

Studying the dependence of superfluid behaviour on the rotational excitation could be a way to gain more insight into the quantum effects in this environment. In order to achieve that degree of control, an optical centrifuge (CF) was proposed to rotate the molecules. An CF is a combination of shaped laser pulses that results in a unidirectional, rotating polarization vector that can accelerate molecules to rotational frequencies of up to 10 THz [22]. It has been used to study molecular dynamics

and properties at extreme levels of rotational excitation and has a degree of control over the excitation unknown to other techniques [31][33]. This degree of control allows us to use molecular rotors as "nano-probes" to investigate the conditions for superfluidity in nanodroplets. The CF would also allow the behaviour to be studied at rotational speeds that could probe a microscopic analogue to Landau's critical velocity [5]. This critical velocity describes the speed at which helium can move and still behave as a superfluid. The dispersion curve of helium reveals that superfluidity will only exist if an object is moving below $58\,\mathrm{m\,s^{-1}}$. This velocity regime translates into rotational speeds on the order of 1 THz, depending on the molecule, and with the precise control over the final rotational frequency achieved using the CF it could be studied.

This work presents two different techniques that can be used to study the superfluid properties of helium nanodroplets. A helium nanodroplet vacuum system was built and characterized for the first time in our lab. After excitation with the CF, the molecules' orientation could be imaged to observe energy dissipation. It is important to implement background subtraction techniques as the density of any helium nanodroplet beam is low, especially in comparison to the high background in our system not normally seen. As well, the spectra of the molecules could be measured to quantify the strength of the helium interactions using resonant ionization techniques. The thesis explains the fundamentals of the rotational excitation scheme, the fundamentals of helium nanodroplet production and important methods for characterization, the detection techniques implemented, and presents some preliminary results with a focus on behaviour in the low signal to background count rate regime. The techniques have been studied extensively with two different linear rotors: CS_2 and O_2, which are also good candidates for observing differences in the weak and strong coupling regimes in the angulon quasiparticle theory. Extending the superfluidity investigation to the high rotational states only possible using the CF would enable the investigation of a quantum rotational analog to Landau's critical velocity. After this technique is developed, clusters of different atoms could be tested for superfluid properties.

Chapter 2

Rotational Excitation Techniques

2.1 Eigenfunctions and Eigenvalues of a Rigid Rotor

The Born Oppenheimer approximation is the assumption that the total wavefunction can be separated into electronic and nuclear components:

$$\begin{aligned} \Psi_{total} &= \psi_{electronic}\psi_{nuclear} \\ &= \psi_{el}\psi_{vib}\psi_{rot} \end{aligned} \tag{2.1}$$

This is a good approximation that is extensively used in molecular physics. The assumption stems from the difference between nuclear and electronic masses, which is about a factor of 1000. There is a mutual attractive force of $\frac{Ze^2}{r^2}$ between an atomic nucleus and an electron which causes the particle to accelerate. Since acceleration is inversely proportional to mass, the electrons experience a much larger acceleration than the nuclei (by a factor of more than 2000). Therefore, the electrons are moving and responding to forces much faster than the nuclei. Because of this, the electronic part can be solved ignoring the nuclear kinetic energy and then used for subsequent computations involving the nuclear terms.

Following the derivation in [2], we can find the eigenvalues and eigenfunctions for a diatomic molecule to understand some fundamental behaviour. The Hamiltonian is broken up into the nuclear term, the electronic term, and the term representing

Coulomb repulsion of the two nuclei:

$$H(r,R) = H_{nuc}(R) + \frac{e^2}{4\pi\varepsilon_0}\frac{Z_A Z_B}{R} + H_{elec}(r,R) \tag{2.2}$$

$$H_{nuc}(R) = -\frac{\hbar^2}{2M_A}\nabla_A^2 - \frac{\hbar^2}{2M_B}\nabla_B^2 \tag{2.3}$$

$$H_{elec}(r,R) = \frac{-\hbar^2}{2m}\sum_i \nabla_i^2 + \frac{e^2}{4\pi\varepsilon_0}\Big(-\sum_i \frac{Z_A}{r_{Ai}} - \sum_i \frac{Z_B}{r_{Bi}} + \frac{1}{2}\sum_i\sum_{j\neq i}\frac{1}{r_{ij}}\Big) \tag{2.4}$$

The Hamiltonian for the electrons includes their attraction for the nuclei and mutual repulsion, respectively. Note, lower case symbols are used to describe electrons and upper case symbols are used for nuclei.

In molecular spectroscopy, the Born Oppenheimer approximation is extended to the electronic, vibrational, and rotational energies because the ratios are related to each other on scales on the order of a thousand. So the energy is written as:

$$E_{total} = E_{electronic} + E_{vibrational} + E_{rotational} + E_{nuclear} \tag{2.5}$$

For a sense of scale, note that pure vibrational transitions are studied using infrared radiation (GHz), whereas pure rotational transitions are studied using microwave radiation (MHz).

The rigid rotor is a very simple system that can be used to describe rotating diatomic molecules. This model is too restrictive to be extremely accurate, but one can still gain a lot of insight into the dynamics of the system. Consider a collection of nuclei of mass m_α located at positions r_α relative to the origin and rotating with angular velocity ω. The angular momentum can be written as:

$$\begin{aligned} L &= \sum_\alpha \mathbf{r}_\alpha \times \mathbf{p}_\alpha \\ &= \mathbf{I}\omega \end{aligned} \tag{2.6}$$

where $\mathbf{I}$ is the moment of inertia. The molecular coordinate system can always be chosen such that the matrix $\mathbf{I}$ is diagonal - this is called the principal axis system.

These matrix elements are:

$$\begin{aligned} I_x &= \sum_\alpha m_\alpha (y_\alpha^2 + z_\alpha^2) = \sum_\alpha m_\alpha r_{x\perp}^2 \\ I_y &= \sum_\alpha m_\alpha (x_\alpha^2 + z_\alpha^2) = \sum_\alpha m_\alpha r_{y\perp}^2 \\ I_z &= \sum_\alpha m_\alpha (x_\alpha^2 + y_\alpha^2) = \sum_\alpha m_\alpha r_{z\perp}^2 \end{aligned} \tag{2.7}$$

Now the angular momentum expression is very simple:

$$\begin{bmatrix} L_x \\ L_y \\ L_z \end{bmatrix} = \begin{bmatrix} I_x & 0 & 0 \\ 0 & I_y & 0 \\ 0 & 0 & I_z \end{bmatrix} \begin{bmatrix} \omega_x \\ \omega_y \\ \omega_z \end{bmatrix} \tag{2.8}$$

as is the expression for kinetic energy:

$$\begin{aligned} E_k &= \frac{1}{2} I \omega^2 \\ &= \frac{L_x^2}{2I_x} + \frac{L_y^2}{2I_y} + \frac{L_z^2}{2I_z} \end{aligned} \tag{2.9}$$

For a rigid, linear rotor that has no net orbital and spin angular moment this is the classical expression for the rotational kinetic energy. If we align the molecule so the bond is along the z-axis and put the moment of inertia at the origin, $I_z = 0, I_x = I_y = I$. For a diatomic, $I = \mu r^2$ where μ is the reduced mass:

$$\mu = \frac{m_A m_B}{m_A + m_B} \tag{2.10}$$

Letting J be the total angular momentum, without nuclear spin, then the Hamiltonian operator is:

$$\hat{H} = \frac{\hat{J}^2}{2I} \tag{2.11}$$

Since we already know the eigenfunctions of the angular momentum operator from other systems such as the Hydrogen atom, we know that ψ_{rot} is described by the

spherical harmonics Y_l^m.

$$Y_l^m(\theta,\phi) = Ne^{im\phi}P_l^m(\cos\theta) \tag{2.12}$$

where N is a normalization constant and P_l^m is an associated Legrendre polynomial. Now we can solve for the energy eigenvalues:

$$\begin{aligned} \frac{\hat{J}^2}{2I}\psi &= E\psi \\ \frac{J(J+1)\hbar^2}{2I}\psi &= BJ(J+1)\psi \end{aligned} \tag{2.13}$$

where we have rewritten the energy eigenvalue, $E_{rot}(J)$, as $BJ(J+1)$ with B as the rotational constant (in J):

$$B = \frac{\hbar^2}{2I} = \frac{h^2}{8\pi^2 I} \tag{2.14}$$

But, the conventional way to express B is in cm^{-1}. Using $E = \frac{hc}{\lambda} = 100hc\bar{\nu}$:

$$B[cm^{-1}] = \frac{10^{-2}h^2}{8\pi^2 cI} \tag{2.15}$$

where c is the speed of light in $\mathrm{m\,s^{-1}}$ and λ is the wavelength in m. It is important to take into account centrifugal distortion since the centrifuge can populate such high J states that even a rigid rotors' bonds soften and we add a correction term to effectively decrease the value of B:

$$E(J) = BJ(J+1) - DJ^2(J+1)^2 \tag{2.16}$$

where D is the centrifugal distortion constant.

2.2 Optical Centrifuge

The CF is an intense, non-resonant field that is used to optically control the rotation of anisotropic molecules. This anisotropy refers to the polarizability of a molecule, or it's ability to form a dipole in the presence of an electric field. This term is really a symmetric tensor, but since we consider linear molecules that have cylindrical symmetry, we can express it in terms of it's polarizability with respect to molecular

symmetry axes: $\alpha_{\parallel} - \alpha_{\perp}$. For linear molecules, $\alpha_{xx} = \alpha_{yy} = \alpha_{\perp}$ and $\alpha_{zz} = \alpha_{\parallel}$. Molecules that have $\alpha_{\parallel} > \alpha_{\perp}$ align to the polarization of the electric field[4].

At a high level, the CF is the interference of two shaped pulses that result in a unidirectionally rotating polarization vector, in the shape of a corkscrew like in Figure 2.1.

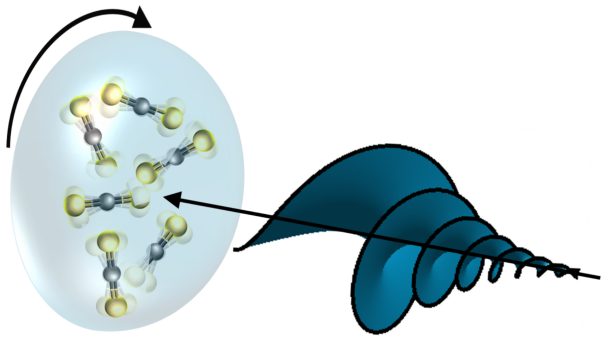

Figure 2.1: The CF field is a linearly polarized field whose polarization vector is rotating with a constant angular acceleration and has an intensity profile that decays. This results in a corkscrew appearance.

To see what that looks like mathematically, we can review the polarization of fields as presented in [3]. First consider a plane wave, propagating in the negative z direction. It can be broken up into it's instantaneous x and y counterparts by:

$$\tilde{E}(z,t) = \tilde{E}_x(z,t)\hat{x} + \tilde{E}_y(z,t)\hat{y})$$

$$\tilde{E_x} = Re[E_x e^{i(\omega t + kz + \eta_x)}] = E_x \cos(\omega t + kz + \eta_x) \tag{2.17}$$

$$\tilde{E_y} = Re[E_y e^{i(\omega t + kz + \eta_y)}] = E_y \cos(\omega t + kz + \eta_y) \tag{2.18}$$

where E_x and E_y are the maximum magnitudes. If $\eta_y - \eta_x$ is an integer multiple of π, the field is linearly polarized. If the two components have the same amplitude, $E_x = E_y = E_0$, and the time phase difference are odd multiples of $\pi/2$ - $\eta_y - \eta_x = \pm\frac{\pi}{2}$, and the resultant electric field would rotate in the xy plane. Right versus left circularly polarized light means that the electric field is rotating clockwise or counter

clockwise, respectively, as seen by the observer. This field would be described by:

$$\tilde{E} = E_0(\cos(\omega t)\hat{x} \pm \sin(\omega t)\hat{y} \tag{2.19}$$

If we take a superposition of right and left ($\pm\hat{y}$ terms) circularly polarized light with equal amplitude, we would recover linearly polarized light:

$$\tilde{E}_R + \tilde{E}_L = 2E_0 \cos(\omega t)\hat{x} \tag{2.20}$$

This is illustrated in Figure 2.2 in the top panel.

In the CF, the two constituent beams are rotating in opposite directions we will also

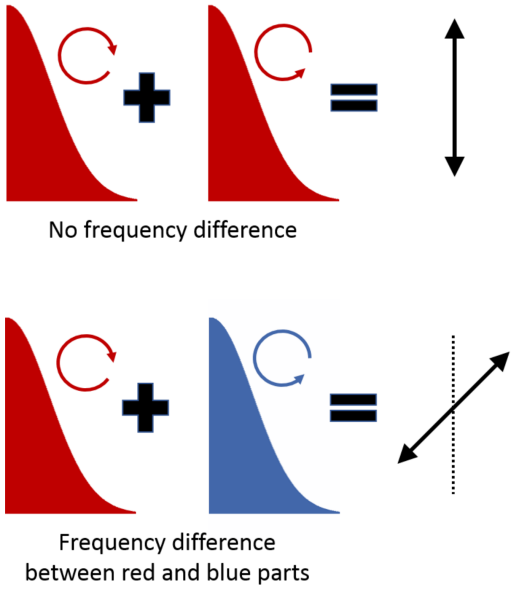

Figure 2.2: An illustration depicting how the circularly polarized fields combine to give the linear polarization (*top figure*) and how the frequency difference between the two circularly polarized fields leads to rotation (*bottom*).

add an offset in the carrier phase, which we will call $\pm\Omega$ [31]. These beams would

be written as:

$$\vec{E}_R = \frac{E_0}{2}\big(\cos[(\omega+\Omega)t]\hat{x} + \sin[(\omega+\Omega)t]\hat{y}\big)$$
$$\vec{E}_L = \frac{E_0}{2}\big(\cos[(\omega-\Omega)t]\hat{x} - \sin[(\omega-\Omega)t]\hat{y}\big) \tag{2.21}$$

When these fields are superimposed, the result is a linearly polarized field that rotates with constant frequency Ω:

$$\vec{E}_{CF} = \vec{E}_R + \vec{E}_L = E_0\cos(\omega t)\big(cos(\Omega t)\hat{x} + sin(\Omega t)\hat{y}\big) \tag{2.22}$$

The time averaged coupling energy a diatomic molecule experiences in a linearly polarized field is given by [14]:

$$V = -V_0\cos^2\theta = -\frac{1}{4}(\alpha_\parallel - \alpha_\perp)E_{CF}^2\cos^2\theta \tag{2.23}$$

where θ is the angle between the molecular axis and the laser polarization vector. Equation 2.23 shows that a molecule perfectly perpendicular to the electric field will not feel the field because of the $\cos^2\theta$ term. It also shows that the potential energy is minimized when $\theta = 0$ and the molecule is aligned to the polarization vector. In order to align the molecule to the polarization vector, the electric field produces a torque which accelerates the molecule with a_{mol}, following [4] and [31]. The torque is the first derivative of Equation 2.23 with respect to θ in the direction towards $\theta = 0, \pi$:

$$\tau = \mathbf{I}a_{mol} = |\frac{dU}{d\theta}| = V_0\sin 2\theta \tag{2.24}$$

where τ is the torque which goes to 0 when $\sin 2\theta = 0$ and this occurs at $\theta = 0, \pi$ (the bottom of the potential well in Equation 2.23). Finally, we have the average angular acceleration imparted to the molecule:

$$a_{mol} = \frac{\tau}{\mathbf{I}} \approx \frac{2V_0}{\mathbf{I}\pi} \tag{2.25}$$

Returning to Equation 2.22, the molecule will align and follow the rotating polarization vector if the acceleration of the CF, a_{CF} is slow enough for the molecule to keep up, i.e. $a_{CF} < a_{mol}$. This means the field cannot start rotating suddenly, as in

Equation 2.22, but must start gradually before beginning the acceleration. In order to achieve this, there must be time dependent terms in angular speed, since $a_{CF} = \dot{\Omega}$. A constant acceleration can be achieved by having the frequency difference of the two fields increasing linearly with time. This is linearly chirping the pulses and adds a quadratic phase factor in the electric field expression. In our case we need the pulses to be linearly chirped in opposite directions, so the fields have quadratic phase factors with opposite signs with respect to one another:

$$\begin{aligned} \vec{E}_R &= \frac{E_0}{2}\big(\cos[\omega t + \beta_R t^2]\hat{x} + \sin[\omega t + \beta_R t^2]\hat{y}\big) \\ \vec{E}_L &= \frac{E_0}{2}\big(\cos[\omega t - \beta_L t^2]\hat{x} - \sin[\omega t - \beta_L t^2]\hat{y}\big) \end{aligned} \tag{2.26}$$

Now when we add the fields, the instantaneous angular speed and acceleration are given by the average chirp rate, $\beta = \frac{1}{2}(\beta_R + (-\beta_L))$:

$$\begin{aligned} \Omega(t) &= 2\beta t \\ a_{mol} &= 2\beta \end{aligned} \tag{2.27}$$

The combined effects of the frequency difference and the counter-rotating circularly polarized pulses leading to a unidirectionally rotating field is illustrated in the bottom panel of Figure. 2.2. We call each of the constituent fields of the CF the "arms" of the CF. From classical mechanics, we know the kinetic energy of a rigid body is given by Equation 2.9 and so $T = \frac{1}{2}I\Omega(t)^2$. As long as the molecule is following the rotating laser field, the rotational energy will increase as the frequency difference between the two interfering fields increases in this classical picture. The power of the centrifuge lies in the degree of control in the rotational excitation. To understand that, we must return to the quantum mechanical description of molecular rotation from Section 2.1 and see how the CF can excite the discretized angular momentum states.

The spectrum of angular momentum states described by Equation 2.16 form a ladder that the non-resonant CF "walks up" via two-photon Raman transitions and this is illustrated in Figure 2.3. The photon from one of the arms of the CF excites the molecule into a virtual, intermediate state and almost immediately another pho-

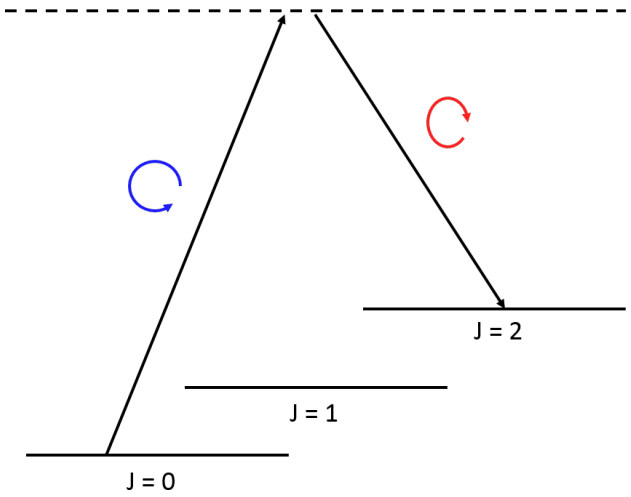

Figure 2.3: Illustration of two-photon Raman transitions that demonstrate how the CF can change the rotational excitation of the molecule with non-resonant processes via a virtual, intermediate state.

ton, from the other arm of the CF, stimulates the molecule back into a lower state. However now the molecule is in a higher rotational state, $\Delta J = \pm 2$, than before the initial photon.

When the initial photon is absorbed and has, say, right hand circular polarization, it increases J by 1 and M by 1 to conserve angular momentum since a photon has spin 1. The next photon with left hand circular polarization causes emission from this virtual state and increases J by 1 again and causes M to lose -1 and the final state is $|J+2, M+2\rangle$. Another way of understanding this increase of 2 is because the polarizability returns to its original position twice for each cycle of the rotating field because there is a factor of 2 between the molecular rotation and the induced dipole. The selection rules for the CF are then $\Delta J = \pm 2$ and $\Delta M = \pm 2$.

Assuming the intensity of the centrifuge field is $10^{13}\mathrm{W\,cm^{-2}}$, the well depth from Equation 2.23 can be calculated for the molecule's shown in Table. 2.1

Molecule	$\Delta\alpha$ (Å^3)	$\lvert U_0\rvert$ (K)	B (cm^{-1})
N_2	0.68	51.6	1.99
O_2	1.07	81.3	1.44
CS_2	8.5	646	0.11

Table 2.1: Molecular information regarding their rotational properties and the effect of the CF on them.

2.3 Impulsive Alignment

An impulsive perturbation to a molecule is a kick pulse which means that it has a duration much shorter than the ground state rotational period of the molecule, $\tau < \tau_{rot} = \frac{\pi\hbar}{B}$ [41]. We work with Gaussian femtosecond pulses to achieve this for light diatomic molecules, so the envelope of the field can be described by $E_K = E_0 e^{-t^2/2\sigma^2}$. These molecules will feel a strong torque towards the polarization direction of the pulse, where the interaction potential is the same as in Equation 2.23 but with $\vec{E_{CF}}$ replaced with the kick pulse field. The torque is still described by Equation 2.24, and from that expression we can see that a_{mol} is proportional to $\sin 2\theta$. Using the small angle approximation we can say that when $\theta << 1$, a_{mol} will be proportional to θ. This means that an ensemble of velocities is created with the excitation and, though the molecules will simultaneously reach $\theta = 0, \pi$, they will continue to rotate after the pulse leaves.

The wavefunctions for a kicked linear rotor are also the spherical harmonics, Equation 2.12. For a linearly polarized kick pulse, the selection rules are $\Delta M = 0$ and $\Delta J = 0, \pm 2$. Here, M is unchanged whereas for the CF $\Delta M = \pm 2$ because of the circularly polarized fields. Since rigid rotors are described by the discrete spectra of Equation 2.16, the ensemble of velocities created from the impulsive perturbation forms a wave packet over the rotational states. The number of rotational J states

populated is proportional to the kick strength, P in units of $\hbar$ [4]:

$$P = \frac{\Delta\alpha}{4\hbar}\int E^2(t)dt \tag{2.28}$$

which holds if the field is below the ionization limit of the molecule. If we solve the integral for our Gaussian field, then the equation for P simplifies to $P = \frac{\delta\alpha}{4\hbar}E_0^2\sqrt{\pi}\sigma$.

Another effect of the discrete rotational spectra is the periodic dynamics of the wave packet. There is a quantum revival effect that is proportional to the second derivative of Equation 2.16. So the full revival time for a linear, rigid rotor is given by:

$$T_{rev} = \frac{1}{2cB} \tag{2.29}$$

assuming there is negligible centrifugal distortion and with B in cm^{-1}. At higher J states, this term should be included. The revival time is one of the most useful parameters for detecting and optimizing the effect because it occurs after the fields are no longer interacting with the system.

2.4 Optical Set Up

The laser system used to perform the CF pump probe experiments was a commerical femtosecond laser from Coherent. The Titanium Sapphire oscillator (Micra) generated broad 80 nm full with half max (FWHM) pulses centered at 800 nm with a repetition rate of 80 MHz. These pulses only have an energy of 5 nJ and are used to seed a Titanium Sapphire amplifier (Legend Elite Duo) that has two stages: a regenerative amplifier and a single pass amplifier. After amplification, the bandwidth decreases to $\approx$30 nm and the repetition rate is 1 kHz. The output power is optimized for 10 W and the pulses had a duration of $\approx$120 ps. Details can be found in [23].

The CF shaper is built according to the proposal from Corkum's group back in the late 90s [22] and is described in detail by our group in [31]. It is based on a common 4f geometry that allows the input beam to be split into components, spectrally, and allows pulses to be arbitrarily shaped in the Fourier transform plane. The 4f geometry is clear in Figure 2.4 from the arrows marked 'f' as the focal length

of lenses L_0 and $L_\pm$. Stretching is typically done utilizing diffraction gratings (GR) and also implemented here. To do nothing to the pulse, these gratings should be set at the focal length of the lenses (points A,B). We play with these distances ($l_\pm$) to impart the appropriate chirp (β) onto each arm of the centrifuge and when these two pulses are combined using a quarter waveplate, the two arms of the CF are then oppositely circularly polarized and counter rotating. Their interference creates a unidirectionally rotating polarization vector with the profile seen in Figure 2.1.

In order to shape the CF further, we place prisms in the focal plane near the

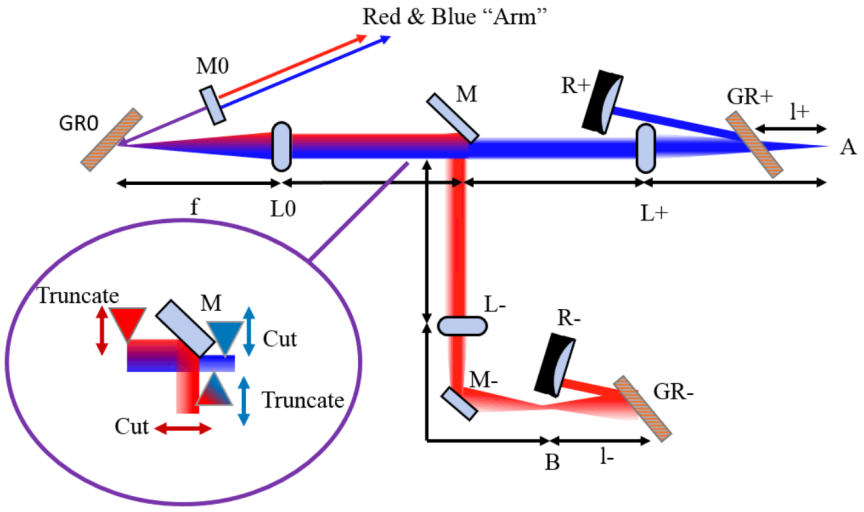

Figure 2.4: CF optical shaper illustrating gratings (GR), lenses (L), and mirrors (M,R) that are set up to produce the two CF arms *Inset:* Truncation and cutting prisms used to modify the CF pulse. Adapted from [31] and [23].

half mirror (M) to modify the CF pulse duration and ability to spin molecules. Previously this was done with a shutter[23], but by placing a few prisms on motorized stages, we have more control over the spectral width and the pulses are precisely reproducible. As well, the prisms do not get damaged by the high intensity at the focal spot. The configuration of prisms around the half mirror is depicted in the inset of Figure 2.4, though the distances from the half mirror are not to scale.

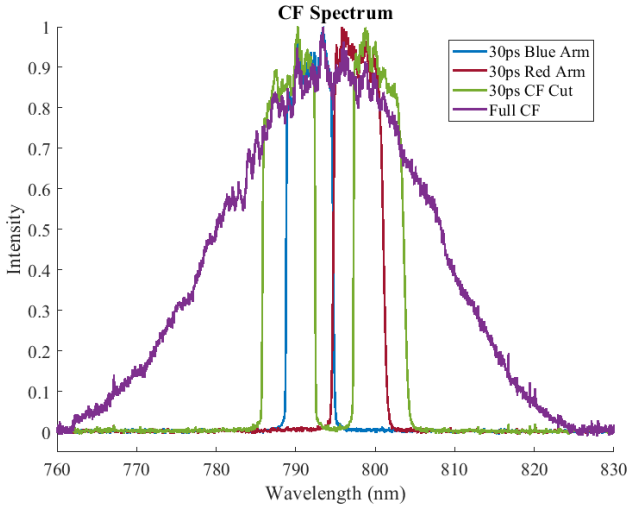

Figure 2.5: Centrifuge field profile in various configurations used during experiments.

The prism that modifies the red (blue) arm of the CF is colored red (blue), and the one that can move in two directions and modify the red and blue arm independently is colored with both. Truncating is done when the prism redirects the spectral components from the outside of the pulse away from the beam. This is shown in Figure 2.5 on both the red and blue arms. Truncation of the CF shortens the pulse duration and limits the final rotational frequency the pulse will reach. It should be done symmetrically (the same in both arms) to ensure efficient rotation of the molecule. "Cutting" is done when the prism redirects spectral components from the center of the pulse. This is also shown in in Figure 2.5, where there is space in the middle of the spectrum. When the CF is cut, the rotational frequency that a molecule sees when the field arrives is higher, and molecules can no long be trapped and follow the field. We call this the "broken CF" because we can match the pulse width and energy of the field but prevent the molecule from rotating. The purpose of cutting the CF is to discriminate against alignment effects due to a strong field when looking for rotation.

By measuring the FWHM position of the intensity profile of the CF in Figure 2.5, the prisms can be moved to give different final rotational frequencies. The positions

of the prisms and calculation of the frequency, energy, and duration (assuming β = 0.31 THz ps^{-1} [31]) is shown in Table 2.2. Aligning the CF with the probe

Spectrum Setting	J ($\hbar$)	Energy (cm^{-1})	Frequency (THz)	Duration (ps)	Red(Blue) Arm Terminal λ (nm)
Full	118	19238	10	101.3	–(–)
10nm/arm	55	4383.1	4.76	48.2	804.5(784.5)
8nm/arm	43	2703.4	3.73	37.8	802.5(786.8)
6nm/arm	33	1607.3	2.87	29.1	800.6(788.6)
4nm/arm	23	792.3	2.08	21.1	798.8(790.0)

Table 2.2: Calibration Table Corresponding to Rotational Frequency, Duration, and Spectral Settings. Note that the duration needs to be calculated using a factor of π in the value of β so $t = 10/(0.31/\pi) = 101.3$.

means aligning three different beams in space and time. The arms of the CF can be aligned independently using the Raman Spectroscopy set up in the lab. Aligning the CF and probe in time can be done to within 1 ns using a fast photodiode in front of the chamber and changing mirrors on the translation stage of the probe. After this, the ion signal of S+ from CS_2 can be maximized within a narrow mass gate with sufficient intensities. To begin with, it is best to set the probe to arrive much later than the CF to ensure that some planar confinement can be observed and used to maximize spatial alignment. This is difficult because the 3 beams ultimately need to be aligned to a sphere that has a 10 µm diameter. If the beams are severely misaligned, it is best to direct them to the far field and reflect them on a wall at the end of the lab. By aligning them to an aperture and to the same spot in the far field, they can be aligned to be quite collinear. Following this, it is best to use a refocusing mirror to simulate the focusing of the beams in the chamber, as shown in Figure 2.6. A pick off mirror is placed in the chamber path and then reflected at an angle off of the refocusing mirror to a CCD camera. The CCD camera is placed at the focal spot of the probe and the CF telescoping optics are adjusted so that it's focal plane is the same as this point. This is shown on the left of Figure 2.6. The CF focal spot

is the top spot and the probe focal spot is the bottom. Once they overlap on the CCD camera, alignment can be optimized using the planar confinement signal. This type of set up is ideal for overlapping two color beams. If only one color is used the refocusing mirror can be replaced with an equivalent lens and the camera can be placed behind this lens. Note that it is important to decrease the intensity using things like neutral density filters and not apertures because the apertures can cause aberrations in the focal spot. The reverse is true when trying to overlap the beams in time because passing through different filtering optics will cause pulse delays.

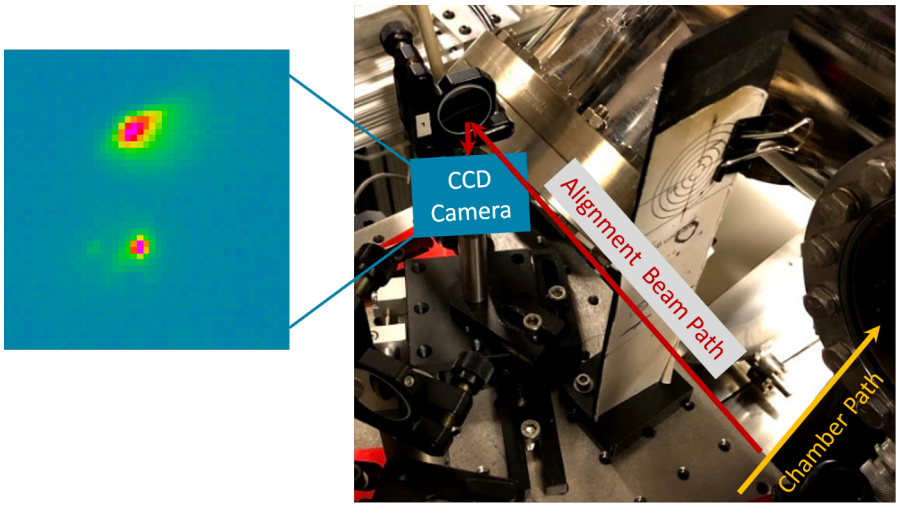

Figure 2.6: CF and probe beam alignment. The CF is ≈10 µm while the probe is ≈5 µm.

Chapter 3

Helium Nanodroplets

3.1 Droplet Formation

Molecules are often cooled via a seeded free jet expansion in order to keep them in a gaseous state and to make them easier to study. Free jet, or supersonic, expansion occurs when high pressure molecules expand through a small orifice into vacuum[53]. This expansion causes the molecules to cool isentropically and even though there is no equilibrium of states we can still describe the process as an adiabatic expansion. This property means there is no flow of heat that occurs between different areas of the expansion and that the specific heats of the gas are constant[51]. The isentropic expansion results in a decrease in the distribution of particle velocities and thus in a decrease of translational temperature, where ≈ 1 K is possible without condensation. Two body collisions, still possible despite the decrease in particle density away from the orifice, further cools the internal degrees of freedom of molecules where a rotational temperature of a few K is attainable[53].

Helium nanodroplets are created by free jet expansion of helium at 20 bar through a 5 µm nozzle cooled to between 10 K to 20 K. The helium gas is pre-cooled in the nozzle before the final cooling process when it expands into vacuum. Initially, the droplet will not be in thermal equilibrium and if it is produced with excess energy, that energy will be removed by evaporating helium atoms. The binding energy between helium atoms is weak; in bulk it is about 7 K, so the temperature

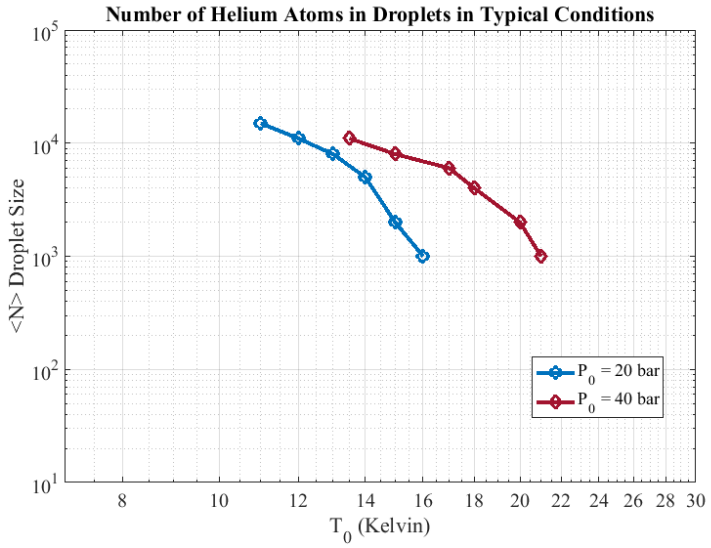

Figure 3.1: Mean size of helium nanodroplets based on different operating conditions controlled by P_0, the backing pressure, and T_0, the nozzle temperature. Adapted from [44].

is adjusted in small increments. Experimental measurements show that the steady-state temperature reached after this evaporative cooling is 0.37 K and is reached in about 0.1 ms after exiting the nozzle. This is interesting because bulk liquid ^{4}He undergoes a phase change from liquid to superfluid at 2.18 K, meaning the viscosity approaches zero. Superfluidity is a special property of bosons, though the fermionic isotope, ^{3}He, can pair up to form bosons and become superfluid below 3 mK as well. Droplets of fermionic helium have been formed, but the steady-state temperature reached is 0.15 K and higher than the superfluid phase transition. ^{4}He is used in order to exploit the superfluid nature of the droplets when studying rotation of molecules and is unique to this low temperature matrix. Using ^{3}He is normally done to clearly contrast the effect of superfluidity seen with ^{4}He.

The droplet formation regime characterized by a 10 K to 20 K nozzle temperature is referred to as subcritical expansion since helium is gas phase before clustering. In this regime, the droplets contain about $1000 - 10000$ helium atoms and have a diameter on the nanometer scale (thus the name "nanodroplets"). The size dis-

tribution has been measured via scattering experiments to be log-normal with the operating point denoted by the mean droplet size, $\langle N \rangle$[21]. In order to change $\langle N \rangle$, one only has to change the backing pressure to the nozzle or the nozzle temperature, according to these experimental measurements, shown in Figure 3.1[45], and normal jet scaling factors[18]. The velocities of the nanodroplets formed in the subcritical regime are expected to lie in the range of $200\,\mathrm{m\,s^{-1}}$ to $400\,\mathrm{m\,s^{-1}}$[7][38], with the mean of the velocity distribution roughly following a $\sqrt{T_0}$ dependence. The velocity distributions are typically quite narrow in this range and $\Delta v/v = 0.02$ is typically achieved.

Molecules are added to the droplets via collisions by adding a gas that fill a different chamber. This is also called a pick up process which is statistical in nature and cannot allow for the droplet to pick up a specific number of dopant molecules precisely. The process is governed by Poisson statistics, with the probability of k molecules being picked up determined by:

$$P_k = \frac{(\rho\sigma l)^k}{k!} e^{-\rho\sigma l} \tag{3.1}$$

where ρ is the number density of the pick up molecule in the chamber, σ is the cross sectional area of the droplets $\sigma = 15.5\,\langle N \rangle^{2/3}$ Å, and l is the length of the pick up chamber. Note that this equation uses the mean droplet size, although there is a distribution of sizes, and that when a molecule is picked up it will transfer its energy to the droplet and evaporate some helium atoms. As long as the droplets are sufficiently large that it can support the lost of ≈ 100 atoms, this equation holds. The molecules that are studied with the centrifuge reside inside the droplet because of favourable energetics, though some dopants can reside on the surface (like alkalis).

3.2 Experimental Set up

Our droplet machine was created by using a vacuum chamber originally designed to create a dense molecular beam. The chambers were inset to minimize the distance between the nozzle and the detection region. In order to turn it into a droplet machine, the nozzle was mounted on a cold head and a gas line was placed in between

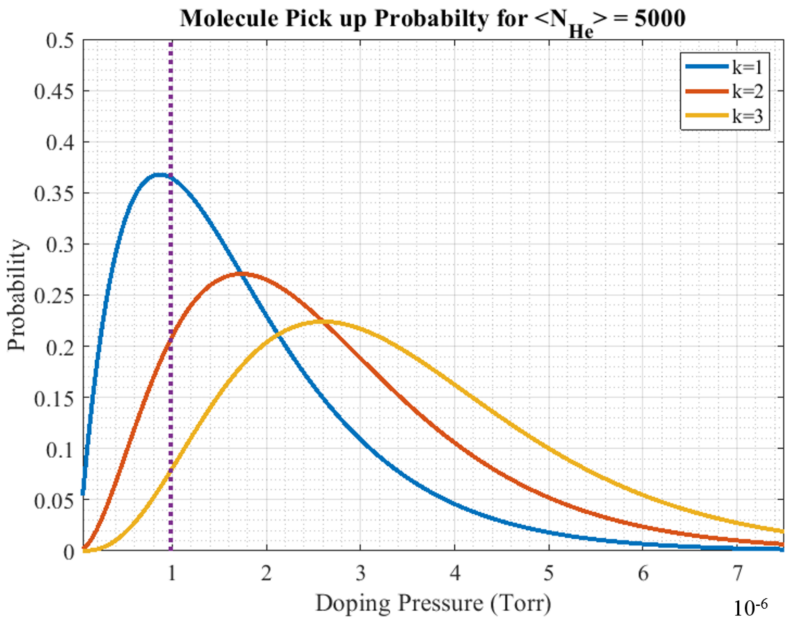

Figure 3.2: Pick up statistics for 1, 2, and 3 molecules. One point of interest is when the doping pressure, $P_D = 9.8 * 10^{-7}$torr, because this is the chamber pressure required to begin picking up 2 CS_2 molecules. This point is shown with the purple dotted line and there is a 21% probability of picking up 2 molecules.

the skimmer and the detection region to allow for doping. The set up we used is depicted in Figure 3.3, but the Residual Gas Analyzer (RGA, SRS 100) that is attached to the end of the Science Chamber is not shown.

The three chambers are equipped with the turbomolecular (turbo) pumps and pressure gauges listed in Table 3.1. The turbos have their fore-vacuum line pumped by an Edwards dry screw pump (iGX600L) which has a pumping speed of 800 $m^3\,h^{-1}$. This pump is placed in a different room and is connected to the pumps via a PVC line with a 4" diameter and 0.1" wall thickness. A stainless steel reinforced PVC hose connects the 4" line to the turbos with KF-40 and KF-25 adaptors (1.5" and 1" diameters). This set up can achieve a pressure of about 50 mtorr to 100 mtorr at the back of the turbo pump, depending on the gas load.

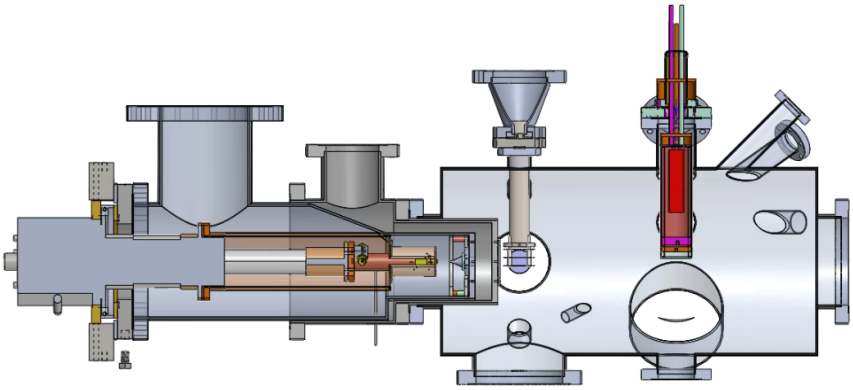

Figure 3.3: Nested vacuum chamber configuration of the droplet machine. Apparatus was designed and assembled for high density molecular jet experiments. Left to right: Source Chamber, Doping Chamber, Science Chamber.

The gas distribution system that connects the tanks and the chamber requires three main components for droplet operation: a line to pure helium (6.0 grade), a line to pump (done with a hermetic scroll pump), and a high pressure regulator. In addition to those components, we have a line connected to oxygen and to a small

Chamber	Turbo Pump	Pumping Speed (L/s)	Pressure Gauge	Pressure Range (Torr)
Source	KYKY FF-200/1300E	1300	MKS 972B Cold Cathode/MicroPirani Transducer	Atmosphere - 10^{-8}
Doping	Pfeiffer TMU 260	260	MKS 500 Cold Cathode Gauge	10^{-2} - 10^{-10}
Science	Edwards D39622000	75	MKS 500 Cold Cathode Gauge	10^{-2} - 10^{-10}

Table 3.1: List of Turbopumps and Pressure Gauges Used.

lecture bottle for seeded gas mixtures in order to perform molecular jet experiments. Many groups do not run any other gas through their nozzle that is used for droplet experiments because it is difficult to the remove the other gas completely and when cooling to 10 K these gases will freeze and clog the nozzle. We have only had one nozzle clog from this, so switching between gases should be done very carefully. Ideally, the lines are pumped and then helium is run through the system overnight before a cool down. Alternatively, a cycle of pumping and purging is done with helium while monitoring the other gas species and helium partial pressures on the RGA. This cycle is repeated three times over 30 min intervals (30 min of pumping, then 30 min purging with helium for one cycle). There should be no increase of the other gas (oxygen for example) on the RGA.

The cold head (Sumitomo 408D2) is mounted onto an adaptor flange that contains an O-ring and allows for horizontal and vertical manipulation. This is shown in Figure 3.4. An O-ring in the ConFlat flange is squeezed between the cold head and a brass square (The ConFlat flange is visible in Figure 3.4, but the O-ring is not since it is on the vacuum side). Brass is chosen because it will more easily slide across the O-ring and stainless steel flange. A thicker stainless steel square, marked with the green arrow in Figure 3.4, is bolted on top of this and has large bolts mounted to its four sides. Loosening and tightening these is what causes translation of the cold head and 3 of them are visible in Figure 3.4 and highlighted with red arrows. The brass housing connecting these bolts to the square can be tightened to fix the cold head's position. The moving parts are made of brass and can actually result in shavings inside the vacuum chamber from rubbing against the stainless steel, but they have not affected the vacuum or caused other damage. A mount designed to attach to the bottom of the cold head manipulator and allow it to slide on to rails. These are also shown in Figure 3.4 and highlighted with the grey arrow. The rails made opening the chamber much easier but also allowed the nozzle height to remain fixed when opening the chamber.

At normal droplet operations, the chamber pressures are shown in Table 3.2

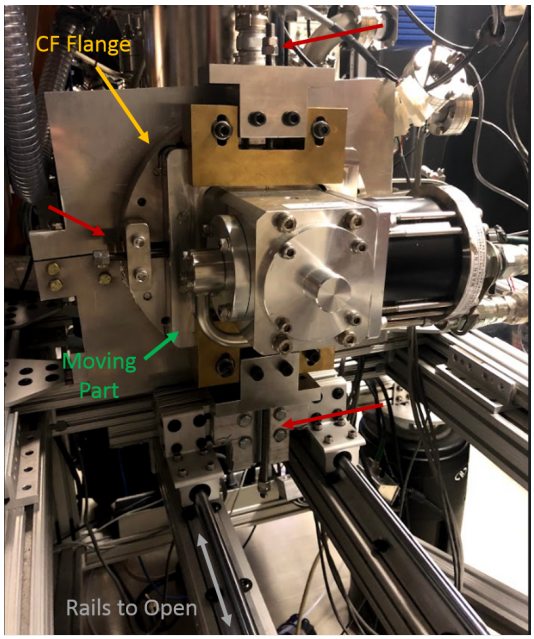

Figure 3.4: Cold head manipulator. The ConFlat flange that contains the O-ring is marked in oragne, the adjustment bolts are marked in red, the square that moves the cold head is marked in green, and the rails installed that pull the ConFlat flange off of the chamber to open the source chamber is marked in grey.

Shutter State	Source Chamber (Torr)	Doping Chamber (Torr)	Science Chamber (Torr)
Beam On	$1.2 * 10^{-4}$	$3.4 * 10^{-7}$	$2.2 * 10^{-7}$
Beam Off	$1.2 * 10^{-4}$	$6.7 * 10^{-8}$	$1.8 * 10^{-7}$

Table 3.2: Normal operating pressures when producing droplets with T_0=14.5 K and P_0=24 bar.

3.2.1 Source Chamber

The source chamber is where the droplets are produced and is the first chamber on the left in Figure 3.3. It is pumped by a $1300\,\mathrm{L\,s^{-1}}$ turbo pump (KYKY FF-200/1300E) and contains the cold head, nozzle, hard drive shutter, and skimmer.

A filter is mounted in between the line and the nozzle to prevent contamination. The nozzle and cryoshield are made of oxygen free copper, which is chosen for it's thermal conductivity at low temperatures. Important design parameters in this chamber include the nozzle flux, the nozzle skimmer distance, the nozzle shutter distance, and the pumping speed. As a rule of thumb, the pressure of the source chamber when producing droplets should not exceed $1 * 10^{-3}$ torr in order to avoid extra heat load on the cold head and to avoid throttling the turbo pump. With our nozzle diameter and pumping speed, this indicates a maximum backing pressure of about 30 bar before the turbo cannot keep up and the beam is destroyed. At normal droplet operations of 14.5 K and 24 bar the source chamber pressure is $1.2 * 10^{-4}$ torr.

The nozzle was fabricated by a collaborating group at the University of Freiburg

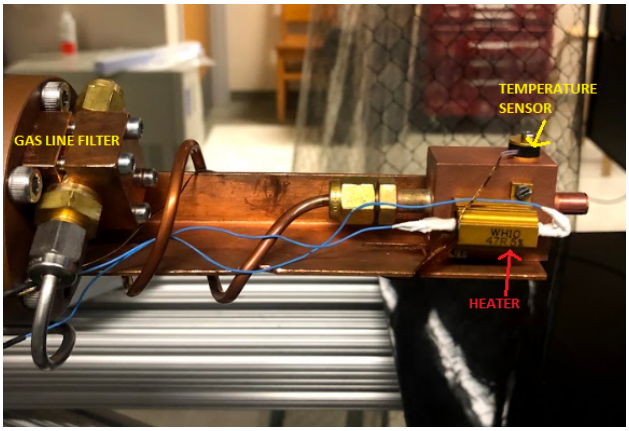

Figure 3.5: Nozzle mounted on the rail, with resistor and temperature sensor attached.

using SEM apertures (Plano EM, Platinum) allowing for a small hole size of 5 µm and is shown in Figure 3.5. They roll the aperture into the end tube that is welded into a square body. This design can tolerate backing pressures of up to 80 bar, though that limit was never tested in our set up since the turbo pump can't tolerate that gas load. This nozzle is received (and stored) in aluminum foil and a desiccant. Installation is straightforward but tricky because the aperture can be clogged so easily - even just from the humid room air. It should not be cleaned like most

vacuum parts with a sonication bath in acetone or isopropanol because this will clog the nozzle. It should be connected to the helium gas line quickly after removal from the desiccant in order to get flow running through the hole to decrease the liklihood that it clogs. After gas is flowing, it is important to check that the nozzle is working and this is done by bubbling the output gas through water. Assuming the output of the nozzle gives an effusive beam through an ideal aperture, the theoretical flow rate through an aperture of this size is $0.011\,\mathrm{mL\,s^{-1}}$ for 1 bar. Linearly extrapolating this to 20 bar, we should measure flow rates around $0.22\,\mathrm{mL\,s^{-1}}$[35]. This can be checked by measuring the volume of helium that bubbles through water in an inverted graduated cylinder, for example. Our tolerance for accepting the nozzle is collecting 10 mL of He in 35 s to 45 s. Even a factor of 2 decrease in this flow rate can result in a lower intensity, but working, molecular beam and a droplet beam that is not operational.

The nozzle is attached to the cold head on top of a rail. It bolts down along the grooves on it's bottom and it's position is etched into the rail using a utility knife. It is very important to place the nozzle at the same distance along the rail because of the potential for beam destruction. Some variance in the angle of the nozzle can be compensated for with the cold head manipulator. On the nozzle's side a $47\,\Omega$ resistor rated for 10 W is mounted and this allows the final nozzle temperature to be controlled. This is done with a Neocera LTC-21 temperature controller that monitors the temperature sensor on top of the nozzle body. Both of these are shown in Figure 3.5, along with the particle filter that is attached to the gas line. Note that the temperature sensor is technically about 10 mm away from the edge of the nozzle but is as close as it can conveniently be. We don't expect this to produce any discrepancies even though the nozzle sticks out from the shield about 2 mm because it should be an accurate reading in steady state conditions.

Another important component of the source chamber is the cyroshield. It is a cylindrical tube that is mounted to the cold head and also actively cooled. It used to shield the assembly shown in Figure 3.5 from the thermal radiation of chamber walls that remain at room temperature. It is a typical design consideration used in most low temperature vacuum designs. The shield is assumed to be uniformly

heated by the outer walls and needs to be made of a material that has high heat conductivity at low temperature (oxygen free copper) to transfer that radiation to a heat sink (the cold head). At normal operations the cyroshield reaches 40 K. Without the cryoshield, the nozzle can only reach 20 K and therefore won't be producing droplets. With the cryoshield the nozzle can reach temperatures as low as 10 K in our set up, depending on the backing pressure. In order to minimize the footprint of the shield, it is made in two concentric cylindrical stages to accommodate the coldhead and the rail that the nozzle is mounted to. There are shims placed at the end of the cold head to make sure the apparatus is long enough to fit around the nozzle assembly. As well, the top part of the first stage has an flat cut in it to accommodate the source chamber profile. On the second stage of the shield, just above the gas line filter, a second temperature sensor is placed.

Because of the chamber geometry, the effective pumping area by the nozzle is very low. This is because there is very little empty space in the cross sectional area. The pump and pressure gauge are on a different end of the chamber from where the expansion takes place. The nozzle expands gas towards a skimmer that is 0.3 mm (Model 2, Beam Dynamics) that is mounted in the center of the the back wall. Ideally, the expansion occurs in an open area of the chamber, away from walls, to avoid reflections and turbulence that can lead to beam destruction. This also ensures that pressure readings are an accurate reflection of the nozzle environment and that the effective pumping speed is maximum.

Prior to installation or during maintenance, it is important to check the conditions of the skimmer and make sure that the tip is shiny and undamaged. This can be inspected with a microscope and a bright light. It is delicate, difficult to mount, and difficult to clean. If the outside is dirty, it can be soaked in acetone or isopropanol and then blown out with nitrogen. It should remain in the chamber as much as possible to avoid dust from landing on it. However, if this happens a thin wire can be pushed through the opening to remove the dust without damaging it. The skimmer and the nozzle are mounted very close together and the final position was determined by checking for a droplet signal (described in Section 3.3) while moving the nozzle closer to the skimmer. The final distance was measured to be

7.6 mm and was decreased from a distance of 10 mm. Moving the nozzle closer to the skimmer meant that more gas would get through the skimmer before there was significant beam destruction which is caused by collisions due to a high chamber pressure and reflections from the back wall. The trade off is how much gain you can get from the free jet expansion and how sensitive your set up becomes to alignment. Our pumping speed is limited in this chamber, so closer was better. The distance between the nozzle and skimmer is difficult to measure accurately because the skimmer is press fit in the wall, the nozzle rail was filed so the nozzle hangs off of it, and the final position depends on how tightly two different flanges are clamped together. The final distance is determined by measuring how far the skimmer mount sticks off the back wall using calipers, using the skimmer specifications from the manufacturer, and measuring the nozzle position from the back rail. It was critical to know this space because a shutter had to be designed to block the beam in this small space.

3.2.2 Hard Drive Shutter

Originally, a DC motor was used but it eventually burned out due to it's inability to radiate heat away in vacuum. This lead us to using an optical hard drive voice coil, as has been done in some groups that needed frequencies of up to 30 Hz with a sharp rise/fall time in vacuum [39]. In our set up, the shutter is difficult to mount in the source chamber because there is no where to attach it, and due to machining tolerances the back end of the source chamber is a bit bigger than the front end. This makes anything that has to be installed very difficult to squeeze in, but may wiggle and be loose at the end of the chamber near the skimmer. Typically, two rings are cut out of acrylic so that one can be pressed up against the back wall and the second can be used to space the shutter away from the skimmer. Although acrylic is normally avoided in high vacuum applications, the source chamber is normally around 10^{-4} torr with the gas load and so the offgassing is not an important consideration in this chamber. In fact, the electrical wiring to the shutter is held to the chamber side with scotch tape and pumping down has never been a problem. The shutter is held together using spacers and brass threaded rod. It is important that bolts on the side that press against the chamber be filed flat so that the shutter moves

perpendicular to the beam path and does not hit the skimmer. The shutter skimmer distance is minimized, since this a more reliable measurement, and is 1.8 mm. The distance from the back wall to the back side of the shutter flag should be 33.5 mm to accommodate this. The shutter and mount are depicted in Figure 3.6. In older designs, a third plate was mounted using a longer threaded rod to help keep the shutter pressed into the back wall. This had to fit around the cryoshield and acted to stabilize the shutter. Since it was very difficult to install and lower frequencies were used, it was omitted from the last round of shutter maintenance.

The hard drive used was a 3.5" drive that was cut to remove the back plate.

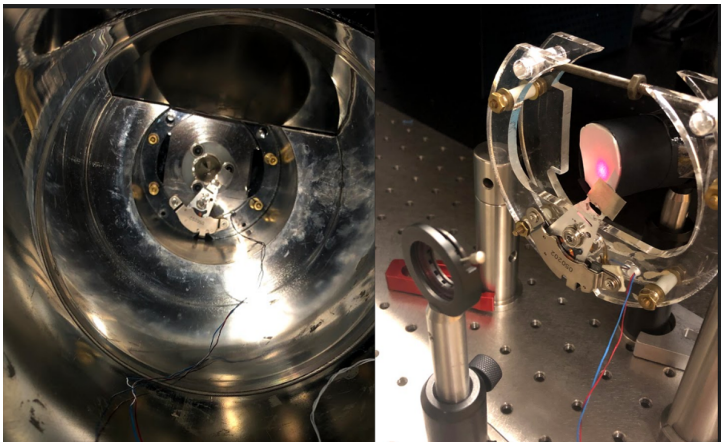

Figure 3.6: *Left:* Shutter mounted in the source chamber in front of the skimmer. *Right:* Shutter mounted to be tested with a HeNe laser beam.

The critical deciding factor in what hard drive to use is the size of the magnet due to the limited space. This was an old Fujitso drive. Most 2.5" drives tend to fit, but were found to overheat at higher frequencies. The shutter was tested to operate at frequencies of 10 Hz to 20 Hz and a control circuit was designed and built by an undergraduate student in the lab to achieve this [49]. This circuit outputs a large initial voltage pulse that decays to a lower holding voltage. The initial pulse provides the high speed to the shutter and the lower holding voltage minimizes the power dissipated by the shutter (details in [49] and [39]). The shutter is normally used at a frequency of 0.1 Hz for applications involving image collection.

The shutter should be centered in the acrylic disks so that the arm and flag open and close with respect to the middle of the chamber, otherwise the beam will not be fully blocked. When assembling the magnet and voice coil from the hard drive to the acrylic mount, the screws need to be undone that align the spacers between the powerful magnets. This makes it difficult to keep the magnet seated properly, though is easy to tell if you have it aligned based on the friction felt when rotating the arm. It is important to get this seated properly, because if it is misaligned extra heat will be generated during operation. This can soften the rubber stoppers, used to prevent recoil, and cause them to move. There are a few critical checks that need to be performed before installing the shutter in the chamber and both have to do with the final assembly. In order to test the alignment, the holder can be mounted concentric to a HeNe laser and the signal read on a photodiode. The beam can be expanded to ensure a large enough flag as well. This is shown in Figure 3.6. The beam size, assuming 45° expansion would be about 10 mm, so this can be visually inspected. Once the position is checked, the shutter can be installed in a rough vacuum chamber; meaning a chamber that reaches a pressure of about $1 * 10^{-2}$ torr. This is enough to see if the temperature of the voice coil raises significantly. If this is left to operate at 5 Hz overnight, it shouldn't raise more than 6^{o}C based on the last round of overnight testing conducted. The shutter can then be placed in the source chamber. If the flange between the source and doping chamber is open and the skimmer is removed, it can be visually inspected whether or not the flag blocks the nozzle. This is also a good time to run the shutter at, say, 5 Hz to ensure the vacuum feed through electrical connections are okay. Finally, the change in partial pressure measured by the RGA can be observed by changing the state of the shutter. The change should be quite dramatic, as shown in Figure 3.7. The rise and fall time is limited by the collection rate of the RGA.

The original hard drive shutter was operated for approximately one year until the magnet casing melted. It was unclear where the extra friction came from. The rubber stoppers may have shifted and caused the arm to heat up the magnet more than normal. The vibrations of the cold head could also have made the arm shift in the

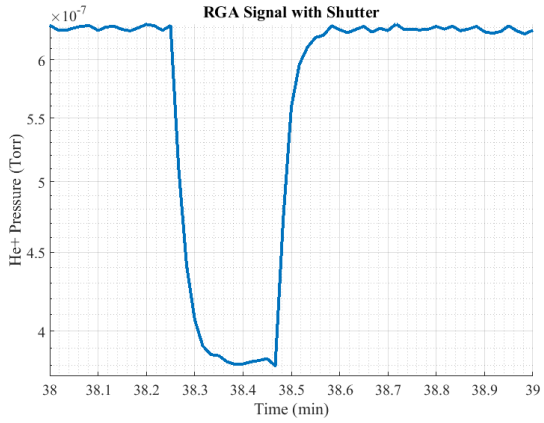

Figure 3.7: Normal Operations of Shutter seen by observing the $M/Q = 4$ partial pressure on the RGA.

holder and cause more friction. The hard drive was simply replaced and the control circuit was reused. Measuring the resistance and voltage drop across the shutter at the control circuit gave the results of Table 3.3 before and after replacement.

Shutter State	Resistance (Ω)	Voltage Drop (V)
Working	9.47	0.85/-0.95
Broken	Overrange	±20.69

Table 3.3: Useful electrical diagnostics for shutter.

3.2.3 Doping Chamber

The skimmer holder mounted in the source chamber is made of Delrin that is press fit into a hole at the back wall. It is made long enough to stick out into the doping chamber. There is a hole drilled into this piece for 1/8" stainless steel tubing to go in. Crack resistance fluorinated Teflon tubing is press fit on top of this and locked in place with a set screw. This is set up is shown in Figure 3.8 with the black arrow

and the Teflon tubing that supplies the doping gas to the beam.

The doping chamber is effectively the backside of the skimmer and the inside of

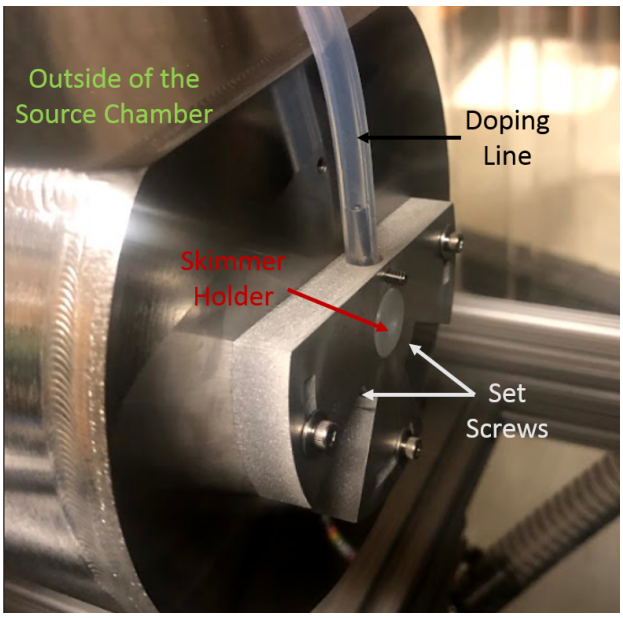

Figure 3.8: Skimmer, doping line, and holder assembled on outside of source chamber.

the holder, as highlighted in Figure 3.9. The holder length that sticks into the doping chamber is 20 mm and has an inner diameter of 11 mm. This creates a high number density of the dopant gas that the beam must travel through and simulates a cell, which is implemented in other set ups. Normally, a small cell is placed in the droplet beam path that is filled up with the dopant gas and localizes it so that it doesn't affect the overall chamber pressure. There is not enough room for this type of construction in the 27.3 mm of space until the science chamber. The gas line pressure can be kept low and adjusted precisely because it is filled with a sapphire crystal leak valve (Varian, 951-5106). The "T" in Figure 3.8 was water jetted to screw into the doping chamber side of the source chamber in order to hold the skimmer holder in place and provide on option for securing the doping line. When the fore vacuum lines were separated there was a pressure differential at the beginning of a pump down

between the source and doping chamber large enough to cause the skimmer to pop out and damage both the nozzle and skimmer.

Placing the doping line right behind the nozzle is also critical in our chamber for producing droplets because when the entire chamber is filled with gas, the number density in the beam path is too low to have a reasonable pick up rate. Mounting the leak valve directly to the chamber is not important either. If it is more convenient to keep it separate it is fine to have stainless steel tubing connecting it to the vacuum chamber. This also allows adaptors that have swagelok connection on the vacuum side so that the tubing cannot pop off with high pressures.

Pumping speed requirements on the doping chamber are such that a pressure difference between $\approx 10^{-6}$ and 10^{-7} torr can be maintained. Without adding any gas for doping at normal droplet operations of 14.5 K and 24 bar the chamber pressure is $3.4 * 10^{-7}$ torr, as mentioned in Table 3.2 and droplet doping conditions bring the overall chamber pressure up to about $5 * 10^{-6}$torr.

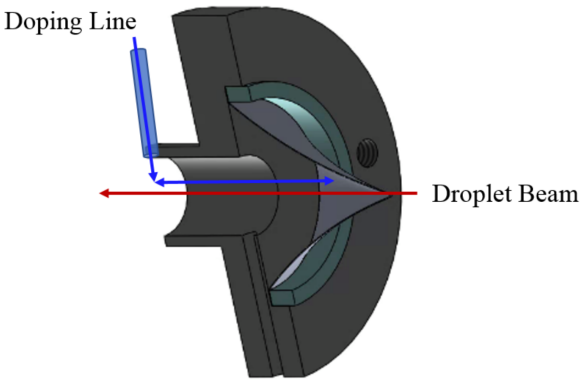

Figure 3.9: The effective doping "cell". The gas line is inserted in the end of the skimmer holder and the doping gas can fill the path marked by the blue area. The droplets can collide with it on the path marked in red and pick up molecules.

3.2.4 Science Chamber

Approximately 31 mm away from the 2 mm aperture separating the doping and science chamber is the laser beam interaction region in the imaging set up. The gas load is much lower in the science chamber since the beam density decreases like $1/z^2$ and the beam has been skimmed already and so the pumping requirements are much lower. At normal droplet conditions with no doping, the chamber pressure is $2.2 * 10^{-7}$ torr. However, with doping due to the proximity to the doping chamber there is a lot of effusive background gas that enters the imaging region. There is no room to place a liquid nitrogen, LN_2, trap between the doping chamber and interaction region, so one was installed another 24 cm downstream. It is used to lower the overall background chamber pressure and mounted to not obstruct the beam from reaching the RGA, which is a Faraday cup detector. It can improve the signal to background ratio by a factor of 3. This chamber will be discussed in greater detail in the next chapter.

3.3 Characterizing a Droplet Beam

Before the beam can be characterized, it is important to check all connections for leaks. After 1 day of pumping, the ConFlat flanges can be checked to make sure the knife edge/copper gasket seal is good. A rough check can be done by looking for pressure increases while spraying acetone at the flange. If the pressure increases, there is a leak and the chamber should be vented so that the flange can be tightened again. A more sensitive check can be done using the RGA. While monitoring the partial pressure of He, a line with a needle at the end can be brought up to the chamber and placed inside the flanges to see if the signal increases. After about 3 days of pumping down, the backing pressure can be increased going from 4 bar to 24 bar, slowly to avoid damaging a turbo pump if there is a large leak. At 24 bar of helium with the nozzle at room temperature, the pressures expected for the source, doping and science chamber is $1.55 * 10^{-5}$torr, $8.6 * 10^{-8}$torr, and $1.47 * 10^{-7}$torr, respectively. In the source chamber, leaks can happen in the gas line connecting the helium tank to the nozzle either for the connections at the flange, filter, or nozzle body. Same with in the doping chamber.

If the nozzle is replaced or if the source chamber is moved, the nozzle alignment should be checked. It can be dangerous to move the nozzle a lot because the O-ring may not seal and will vent the chamber with atmospheric gas. Nozzle alignment can be observed with a decrease in source chamber pressure and increase in science chamber pressure, but we can more precisely monitor the quality of alignment using the RGA at the end of the chamber. The pressure increase is very dramatic - over two orders of magnitude from absolute pressures of 10^{-9} torr to 10^{-7} torr. Once the signal is maximized it's important to check the sensitivity of the maximum to translation. For our manipulator, moving the nozzle up/down or left/right by 1/4 of a bolt rotation should take the signal decrease to half of the maximum. When the nozzle or skimmer are partially clogged, this changes drastically and the nozzle-skimmer alignment is very sensitive to movement.

Once these checks are passed, the nozzle is ready to be cooled. The source, doping, and science chambers are monitored with respect to the nozzle temperature as well as the He and He_2 pressures on the RGA. As the metals contract, there is movement of the nozzle with respect the the skimmer and seen quite dramatically in our chamber. It is a bit more dramatic due to the small nozzle - skimmer distance, with respect to other group's chambers. This can be seen in Figure 3.10 in the yellow Science Chamber pressure curve between 100 K to 200 K. Once the nozzle

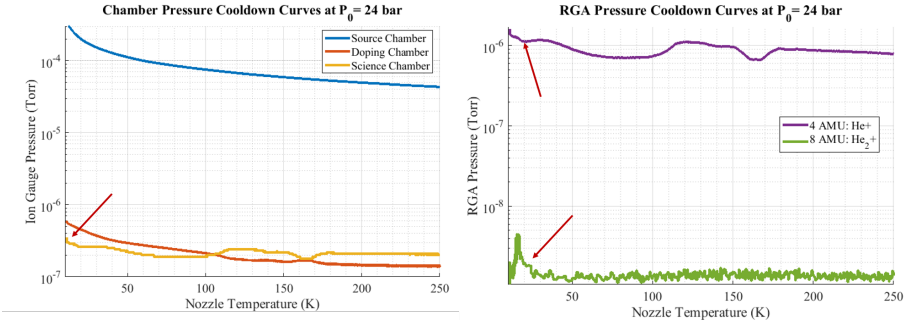

Figure 3.10: *Left:* Chamber Pressure Cool down Curves *Right:* RGA Pressure Cool down Curves.

temperature reaches about 20 K the flux of He decreases (beginning of clustering)

and the science chamber pressure and He RGA signal decrease. Most importantly, He_2 begins to form and is the important benchmark for droplet production since it can only form from droplets. As showing in Figure 3.11, it is 0 up to about 20 K. As the nozzle cools more, droplets begin to form and these pressures should increase quite dramatically as larger and larger clusters are produced. A clear increase is seen in the curves shown in Figure 3.10 at low temperatures and is marked with red arrows. It is not as dramatic because of the misalignment that happens during cool down and because of the limited pumping speed that results in a higher overall chamber pressure. This is shown in Figure 3.11 in comparison to the expected droplet behaviour seen in other chambers[8]. The lowest dip in pressure, marked by orange arrows, is when droplets start to form. This is proportional to $\sqrt{P_0 d}$ and just shifts to colder temperatures for our set up, but the qualitative behaviour should be the same. In our chamber, we do not see a clear maximum around 30 K, marked with green arrows, before the helium clusters into droplets, but we do see a dip and then subsequent rise in pressure that also corresponds to an increase in the He_2+ signal. We see the He_2+ signal dips after rising, which is not expected, as a result of misalignment and beam destruction from the high chamber pressure. This is fixed by realigning the nozzle and skimmer at the peak around 13 K. The increase in signal after the dip is marked by red arrows and is when helium droplets start to form.

Figure 3.12 shows the partial pressure of He_2 and He after the nozzle is aligned and the increase is more clear. Different backing pressures were supplied to the nozzle, which shows how the droplet formation temperature increases with higher backing pressures. When the turbos start to be throttled or there is beam destruction, the increase abruptly stops as is seen for the curves of He at $P_0 = 20$ bar and 24 bar. As well, the lowest temperature achievable increases with an increase of backing pressure which is likely a result of extra friction from the additional gas.

The nozzle should be aligned to the maximum flux into the science chamber at the desired operating temperature and it can take up to 20 min for the signal to stabilize. The heater can be turned on to maintain the nozzle temperature to within ± 0.1 K but can take up to 1 min to stabilize when changing the shutter state between on and shutter off. When the nozzle is clogged, the shutter state between on and off

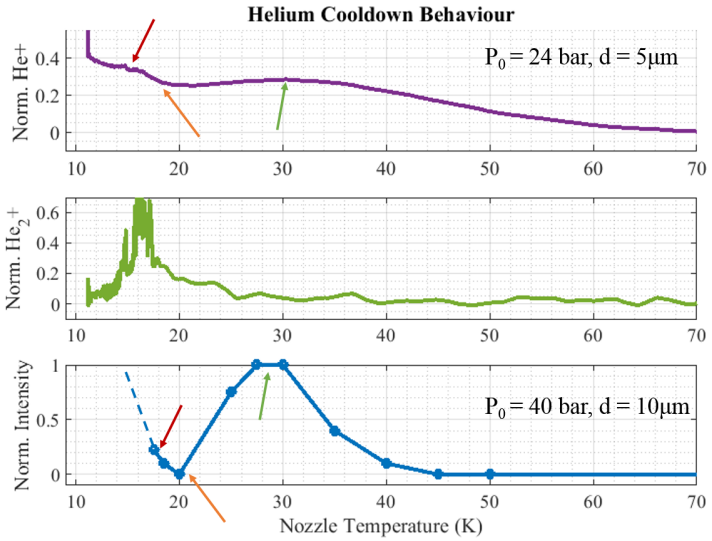

Figure 3.11: Comparison of our RGA Partial Pressures (normalized) with the droplet signature seen in other chambers, shown in the lowest panel. Adapted from [8].

becomes less square, as shown in Figure 3.13, and will be very erratic. Heating the nozzle does not work and the chamber has to be opened for maintenance if this happens.

The fragmentation in the time of flight spectrum can be observed with the femtosecond probe at high intensities. This is done using the probe because an electron gun is not available for comparison to literature; 100 eV is often used in comparison to the 1.5 eV per photon we have to reach the ionization energy of He at 24 eV. The time of flight signal observed in our chamber shows cluster peaks up to about 16 AMU with probe intensities that begin to reach the limit of damaging the detection equipment. In other set ups, helium oligomers can be a concern (for background) up to 32 AMU. Our time of flight spectrum is shown in Figure 3.14. The peak at 18 AMU is just background water and not due to the droplet beam. It is clear from the non-linear increase in ion signal with probe energy that there are some droplets that are ionizing from plasma ignition and is an indication of droplets forming[20].

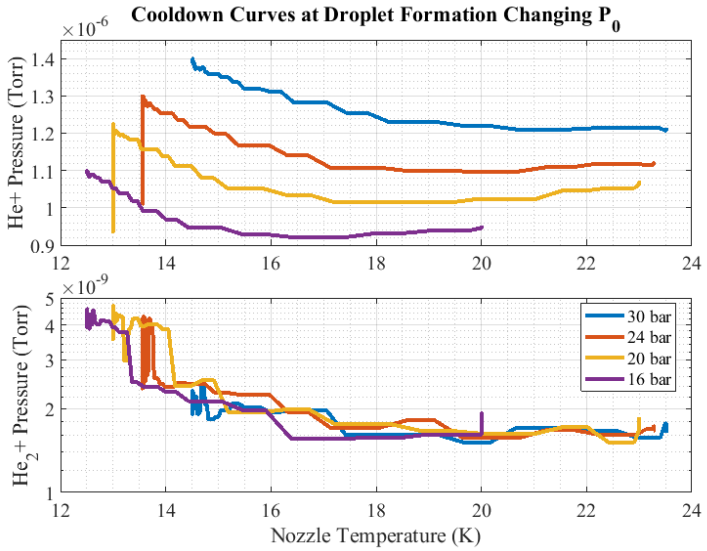

Figure 3.12: The effect of changing the backing pressure on the cool down curve. The effect is a change in the coldest temperature that can be reached in the system. Pushing this system to operate at colder nozzle temperatures results in producing larger helium droplets and a larger pressure load in the source chamber. We are at the limit of throttling the turbo pump and it can be seen that the beam starts to be destroyed with the jumps down in pressure for P_0 = 20 and 24 bar.

It is unclear what impact our inability to produce larger helium fragments has on the beam quality. It could suggest that we have fewer droplets successfully clustering in our beam which would lead to a lower count rate than anticipated. The ratio of the the peak heights can be evaluated from the curve ionized with 100 µJ of probe energy to compare against other experiments where the intensities were measured using an electron gun and is shown in Table 3.4. The ratio of He_8 to He_{12} is comparable, but the other ratios are off by an order of magnitude. It is more important for us to efficiently produce medium - small droplets (< 5000) because it can be difficult to ionize molecules inside large droplets and because of collisional effects that prevent us from determining the molecular position. This will be discussed in the next chapter.

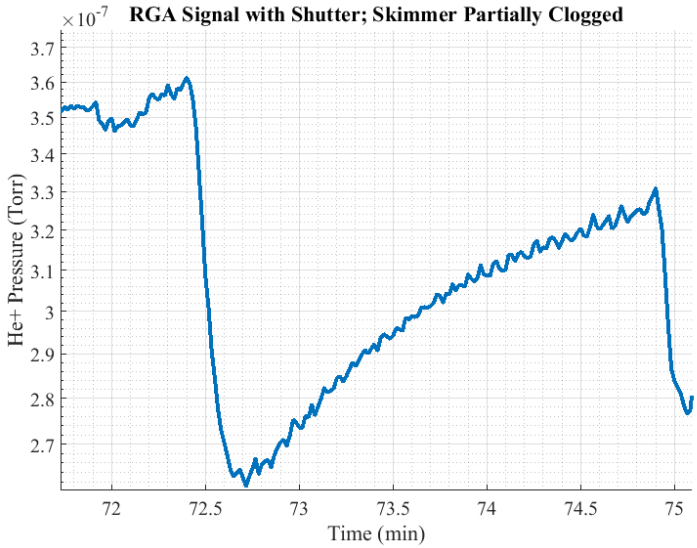

Figure 3.13: Partial Clog of Skimmer: the shutter switched from beam on to beam off at 72.5 min and remains off. We do not observe the anticipated square wave.

Experiment	I_8/I_{12}	I_{16}/I_8	I_{16}/I_{12}
Vilesov	6.7	0.027	0.294
UBC	3	0.67	2

Table 3.4: Ratio of Peaks; comparing our measurements to another experiment at 14 K found in [45].

The final check to verify that droplets are being produced, and that they are being doped effectively, is to measure the CS_2 dimer signal. Dimers form inside the helium droplets or in a seeded gas expansion when they get cold[37]. They are detected by observing CS_2 molecule repulsion in an ion image, as shown in Figure 3.15. Without droplets in the Beam Off image, only background CS_2+ is observed. The line at the right is the effusive jet that forms from the 2 mm aperture

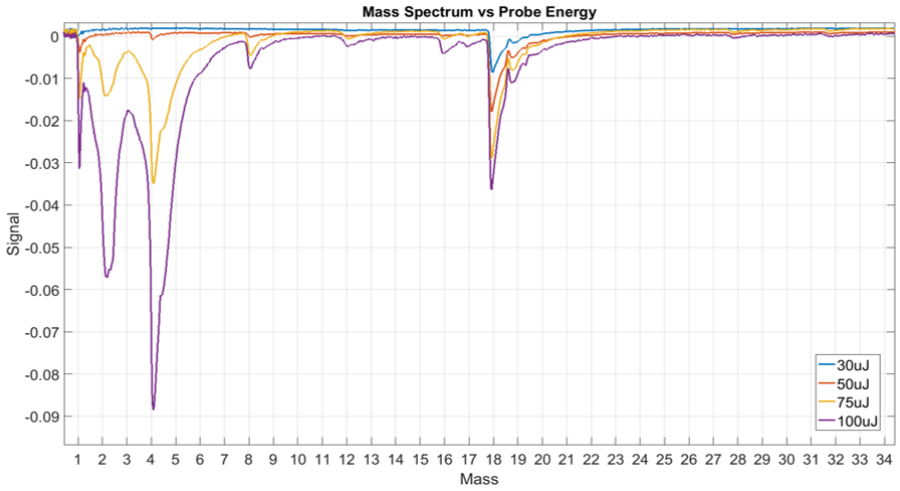

Figure 3.14: Droplet signal TOF for various probe energies.

leading to the science chamber. A circle is expected because the molecules are oriented isotropically when ionized by the probe. The asymmetry is because the detector is overwhelmed by the strong signal or partial damage and is not responding linearly. With droplets in the Beam On image, ions are detected out to the large blue ring, which marks the expected repulsion energy.

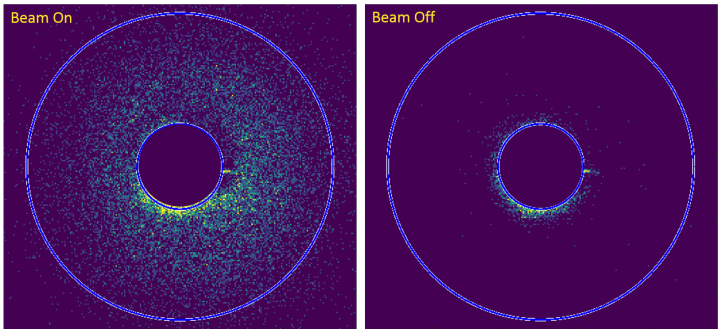

Figure 3.15: CS_2 Dimer Doping 13.6 K at $P_D = 1 * 10^{-6}$ torr.

3.4 Molecular Jet Dilution

The number density of a doped droplet beam is significantly lower than the density of a pure molecular jet. The two can be compared using the formula for number density, $n = F/vA$, and the flux of a beam, $F = \Delta PS/k_B T\Omega$ [44]. Combining the two and taking the ratio for the number density between two species yields the following formula:

$$\frac{n(X)}{n(Y)} = \frac{\Delta P_X S}{v_X A k_B T \Omega} \frac{v_Y A k_B T \Omega}{\Delta P_Y S} = \frac{\Delta P_X}{q_X v_X} \frac{q_Y v_Y}{\Delta P_Y} \tag{3.2}$$

where n is the density, v is the velocity, A is the area of the chamber, F is the flux, S is the pumping speed, and Ω is the angle subtended at the end of the chamber by the aperature and skimmer. If we take the ratio of $n(O_2)$ and $n(He_n)$, the molecular jet and singly doped beam densities, we don't care about A because it is the same. The flux of molecules is given by the pressure increase, ΔP, corrected for the sensitivity of the ion gauge, q. The velocity of the oxygen jet is $736\,\mathrm{m\,s^{-1}}$ and the droplet beam velocity depends on the exact operating point, but we can calculate using $476\,\mathrm{m\,s^{-1}}$. The speeds are taken from the St. Venant Wantzel equation:

$$v = \sqrt{\frac{2k}{k-1}\frac{k_B T}{M}} \tag{3.3}$$

where k is the adiabatic exponent or ratio of specific heats (5/3 for monatomics, 7/5 for diatomics, and 4/3 for triatomics), k_B is the Boltzmann constant, T is the temperature, and M is the mass. This form of the equation assumes the gas expands into perfect vacuum. At the operating conditions we expand the helium at, we should be producing clusters of 5000 atoms and assuming the doping is set according to Poissonian statistics, 30% of those nanodroplets contain a single oxygen molecule. When we calculate the ratio from Equation 3.2, we get $\frac{n(He_n)}{n(O_2)} = 0.0053$, which is close to the same values from other nozzles used in this chamber. Clearly this poses a challenge in terms of collection since the signal density is ≈ 2 orders of magnitude lower than a molecular jet of pure oxygen, and simultaneously the added doping gas will lower the S:B by 3 orders of magnitude. This number isn't terribly useful to diagnose the beam, but it gives a good indication for how to simulate the number

density of a droplet experiment. It also highlights the importance of beam alignment and minimizing beam destruction, since the pressure increase is the important factor in number density and not overall chamber pressure, although they are related.

Because of the CS_2 and He dimer signals, we are confident that we are producing doped helium droplets. The other metrics suggest that we are not producing them as efficiently as conventional set ups but there is no scaling parameter to help us determine by how much. By producing CS_2 doped droplets, preliminary results were able to be measured and explored.

Chapter 4

Detection Techniques

4.1 Velocity Map Imaging

An ion focusing scheme is utilized that maps different initial velocity vectors onto different points of a detector plane when the probe ionizes the molecule, known as velocity map imaging (VMI) [13]. The three dimensional velocity distribution may be recovered from the two dimensional ion image and allows the molecule's rotational energy and orientation to be inferred. Ions are created through laser induced Coulomb explosion, which is a process that rips electrons from a molecule rapidly with an intense probe pulse. This creates a positive, highly charged "parent" molecular ion that fragments from the huge Coulombic repulsion the ions experience after the electrons are ripped away. The axial recoil approximation assumes the fragment ions recoil along the bond axes of the parent molecule, which allows the molecular orientation to be inferred[11][41]. Different ion fragments can result depending on the charge of the parent molecule and these break up via different pathways, or channels, creating distinct rings in an ion image due to different amounts of energy released. These rings are used to determine the transitions of the excited molecule and thus the VMI technique allows insight into these parameters where conventional time of flight (TOF) methods do not[12]. We use VMI to monitor the orientation of a molecule excited by the CF because the rotational excitation pulls the molecule into the plane of rotation. We compare a bare molecule's angular distribution to the angular distribution from inside a helium nanodroplet. Changes

in the distribution would allow insight into the coupling strength and degree of superfluidity of a nanodroplet.

A basic VMI consists of a three electrode set up: a repeller plate V_R, an extractor plate V_E, and a ground plate, as shown in Figure 4.1. The extractor and ground plates have open holes in the center to allow the ions through while the repeller is a closed disk that provides a uniform field to accelerate the ions. The ions are accelerated to a multichannel plate (MCP Tectra, MCP-50-D-FV-P46) that creates a cascade of electrons that then hit a phosphor screen. A photomultiplier tube (PMT) can be used to collect this ion signal and is useful for TOF measurements. As well, the light is focused onto a CCD camera sensor with a 40 mm condensing lens and this allows the ions to be tracked via pixel locations. The voltages applied to the electrodes are always in the order $V_R > V_E > 0$ and the ratio V_E/V_R is fixed depending on the geometry of the electrodes. This ratio fixes the focal plane and the shape of the trajectories are independent of the mass to charge ratio, m/q. So, any two particles that are created at the same point with the same kinetic energy and velocity vector will follow the same path though their TOF will be different if they are different masses [13][6]. This means that an energy scale can be applied to the image radii that is independent of the mass and can be extended to other masses.

In order to recreate the full three dimensional velocity distribution, an inverse Abel transform must be done. This is a unique transformation that can map between 2D and 3D velocity distributions as long as there is cylindrical symmetry and what is done to reconstruct the full 3D distribution. This is not always possible to attain cylindrical symmetry and it has become common practice to use the raw ion image and characterize the alignment from the 2D distribution[47]. The raw ion image can still be used to recreate the 3D distribution if "time slicing" is implemented[46]. This means gating the MCP and only collecting ions that arrive within a certain, very narrow, time window. Ideally, this time window correlates to one shell of the 3D velocity distribution from the Newton sphere and improves the resolution. We used this principle to extract the ions in the middle of the TOF peak and increased the resolution of the distribution.

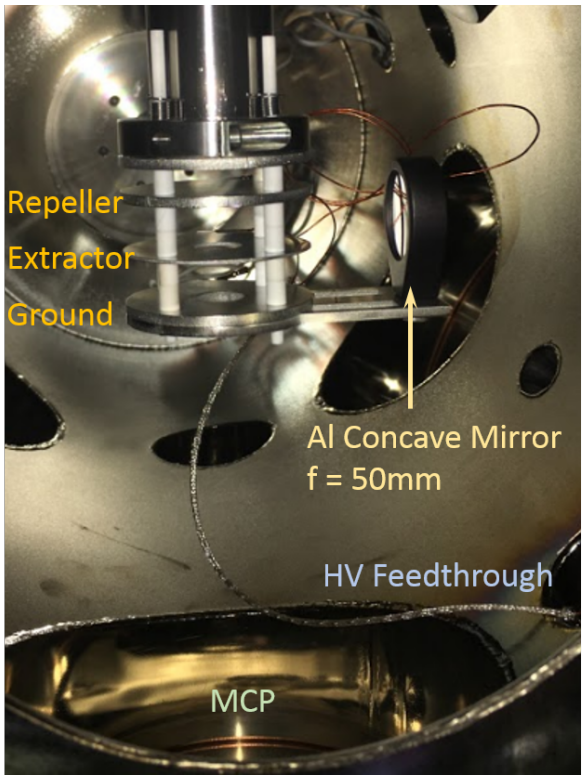

Figure 4.1: VMI Configuration.

A few general relationships are outlined in [6] and are useful to recall here. When ions are created in a VMI, they will give rise to a spherically symmetric cloud that expands at a velocity, v, and will create a ring on the detector with radius, R, called the Newton Sphere. R is related to the t_{TOF} by:

$$R = Avt_{TOF} \tag{4.1}$$

where A is the magnification factor and depends on the specific VMI geometry. As in conventional time of flight mass spectrometers, t_{TOF} is determined by the initial acceleration set by the repeller voltage[6]:

$$t_{TOF} \propto \sqrt{\frac{m}{qV_R}} \tag{4.2}$$

The velocity can be expressed as the kinetic energy release $E_{KE} = \frac{1}{2}mv^2$ and can be substituted into Figure 4.1 to show how the radius scales[6]:

$$R \propto A\sqrt{\frac{E_{KE}}{qV_R}} \tag{4.3}$$

4.1.1 Velocity Map Imaging Calibration

The ratio for our set up was determined to be 0.718 (V_R = 4500 V and V_E = 3230 V) experimentally. The MCP and phosphor screen voltages are set to 800 V and 4100 V to 4500 V. These were decided by finding a linear regime of operation by monitoring the increase in ion response as the voltages were increased and staying withing the limits of operation. Using a molecule with known Coulomb channels, such as CS_2 which releases about 3 eV per S+ fragment[48] or N_2 with 4.8 eV per N+ fragment[52] (the exact energy depends on the intensity of the pulse), ions are created using a probe that is polarized perpendicular to the TOF so that there is an anisotropic ion distribution. This distribution is illustrated in Figure 4.2 for N_2. V_R is then determined such that the size of the distribution fills the detector in order to maximize the spatial resolution that can be achieved with the sensor or can be selected in order to optimize mass selection with the TOF. After, V_E is changed to optimize the ion focus which means maximizing the ion signal and making it as sharp as possible. V_R is also important because it determines the energy at which ions impinge the MCP and this changes the collection efficiency. Typically, the best achievable efficiency is 65%[34].

Once the voltages are fixed, the arrival time of the ions can be scaled to allow for mass gating of the MCP. Mass gating is done using a high voltage trigger (Photek, GM-MCP-2) that pulses the back of the MCP up an additional 500 V from what the power supply is set to (800 V+500 V) in order to turn the detection on. Although the trigger can be set to 10 ns, we are limited to a gate as narrow as 20 ns because of the pulse generator and coupling into the system. The calibration of this gate requires knowing two different masses; an easy selection is the ionization of N+, as shown in Figure 4.2, and it's parent ion N_2+, which will just be a bright spot.

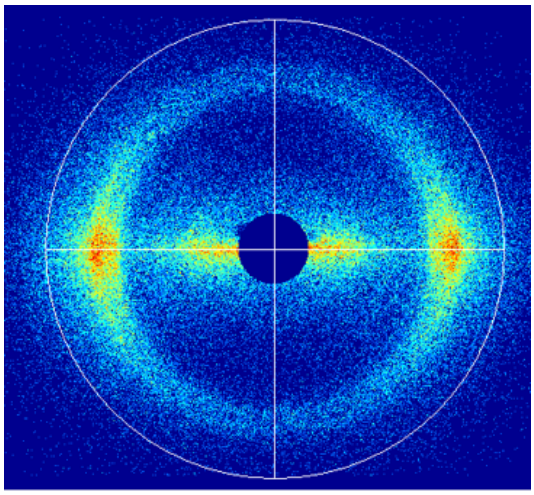

Figure 4.2: N+ ion distribution for a probe polarized perpendicular to the TOF path. The circle had a radius of 250 pixels. The ions were created by ionizing a jet of N_2 expanded at 20 bar with the fs probe set to an intensity of $2.1 * 10^{15} \mathrm{W\,cm^{-2}}$ and the VMI set at V_R = 4500 V, V_E = 3230 V, V_{MCP} = 800 V and the Phosphor Screen = 4300 V.

In principle, it's important to use a probe that is polarized parallel to the detection plane to avoid having to select between ions that are accelerated towards the plane and away from the plane (forward and backward ions) as would be the case with a probe that is polarized parallel to the TOF path. This isn't very important for our set up because at V_R = 4500 V the difference in arrival time between the forward and backward ions made from N_2 is expected to be 18.8 ns (from SIMION simulations of our VMI detector) but the smallest mass gate possible is 20 ns. It is also important to note that there can be a background signal from water that hasn't been completely pumped out of the chamber, M/Q = 18 AMU. We can distinguish this ion signal from the N_2 related signal using the shutter.

We can set a simple time calibration for M/Q from the TOF at a specific repeller voltage by scaling the time axis with the assumption $t_{TOF} \propto \sqrt{M/Q}$. From $t = 0$ in the MCP trigger, there can be some dead time, which means there is an offset that needs to be accounted for. We use two known masses to fit $M/Q = A(t_{TOF} + B)^2$, where A is the scaling factor and B is the offset ($M = 0$ corresponds to $t_{TOF} = B$). If

we use two data points, $(t_{TOF}, M/Q) = (L_X, L_M)$ and $(t_{TOF}, M/Q) = (U_X, U_M)$ we can solve for A and B as follows:

$$L_M = A(L_X + B)^2$$
$$A = \frac{L_M}{(L_X + B)^2} \tag{4.4}$$
$$U_M = A(U_X + B)^2$$
$$B = \sqrt{\frac{U_M}{A} - U_X} \tag{4.5}$$

Substituting Equation 4.4 into Equation 4.5 and isolating B:

$$B = \sqrt{\frac{U_M}{L_M}}(L_X + B) - U_X$$
$$B = \frac{\sqrt{\frac{U_M}{L_M}}L_X - U_X}{(1 - \sqrt{\frac{U_M}{L_M}})} \tag{4.6}$$

Finally, Equation 4.6 can be used to solve for A from Equation 4.4. Normal practice is to assign the lower mass to be $L_M = 14$ for N_+ and the upper mass to be $U_M = 28$ for N_2+. Then, for L_X and U_X we record the leading edge of the MCP trigger (set to the narrowest gate possible, 20 ns) and calculate A and B for the available trigger range. For a fixed set of voltages, an energy scale is assigned to the image radii that is independent of the particle mass and once this is done for one species, the calibration would apply for all other masses. We assume that we can scale the radius of the ion image in a simple way according to[6]:

$$E_{KE} = C(qR^2) \tag{4.7}$$

where C is the scaling factor that we need to determine. Note that this C is valid for one V_R and would need to be remeasured for different electrode voltages. Normally, this is done using a well known photoelectron energy channel. We do not have the ability to measure photoelectrons because a flight tube was not installed that would shield the electrons from stray electric and magnetic fields, so we had to use a well known ion kinetic energy release channel. Another group tested their

photoelectron calibration versus their calibration according to the dimer repulsion felt by two CS_2 molecules, and we implemented this procedure [37]. It is important to do this after the mass calibration is known because the CS_2+ signal comes from a seeded jet and can be weak (and the dimer signal weaker) and data collection has to be done over a long period of time, up to 30 min to 45 min to see a signal. The following ion image was collected using a probe pulse parallel to the TOF path (for cylindrical symmetry) with the mass gate set to $M/Q = 76$ AMU and is shown in Figure 4.3. The radial distribution is found with respect to the center of

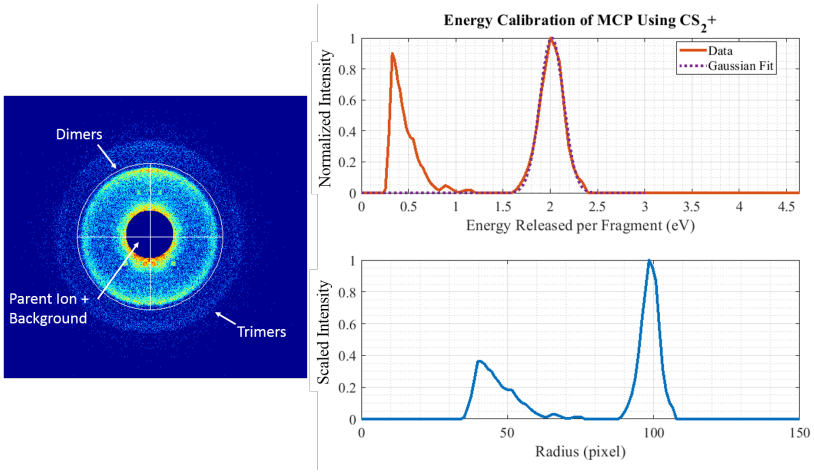

Figure 4.3: Determining the scaling in $eV/pixel^2$ for CS_2 dimers.

Coulomb energy (CE) and is plotted in the bottom right of Figure 4.3. The center is considered the point of maximal intensity of the parent ion because this process has no kinetic energy release and therefore no repulsion. As well, background CS_2 can build up in the chamber. These are removed from Figure 4.3 because they are much brighter than the dimer ring, which is plotted on the left. It is not important for the energy calibration, but the outer ring indicates trimers that are known to cluster in these experiments as well and it should not be mistaken for the dimer ring. We find the peak of the outer ring in the radial distribution, which is 98.44 pix, and assign it to the 2 eV of kinetic energy release expected by the dimers. This gives a scaling factor of $C = 2.064 * 10^{-4}\text{eV}/pix^2$ for $q = 1$. This scale is applied to the radial distribution and then plotted in the top right of Figure 4.3. As well, the

intensity is scaled by the radius so that $I \rightarrow I/R$. The resolution can be determined by fitting the scaled distribution to a Gaussian and using the standard deviation of the fit: σ =0.2 eV (equivalently, 6.5pix). The resolution would then be reported as $\Delta E/E = 20.5\%$ ($\Delta R/R = 7\%$). For reference, other detectors typically have resolution $\Delta E/E < 5\%$[26][54]. The specifications for our set up that have been experimentally determined and/or simulated are summarized in Table 4.1.

Feature	V_R =4500 V	V_R =2500 V
Simulated Resolution	$\Delta E/E = 10.6\%$ ($\Delta R/R = 4\%$)	$\Delta E/E = 4.5\%$ ($\Delta R/R = 3\%$)
Experimental Resolution	$\Delta E/E = 20.5\%$ ($\Delta R/R = 7\%$)	N/A
Scaling Factor [eV/pix^2] Scaling Factor [(m s^{-1})/pix^2]	$C = 2.064 * 10^{-4}$ for $q = 1$ $C = 22.89$ for $q = 1, M = 76$	$C = 1.391 * 10^{-4}$ for $q = 1$ (sim) $C = 18.79$ for $q = 1, M = 76$ (sim)
Simulated Energy Acceptance	23 eV	13 eV
Maximum Radius	300 pix	300 pix

Table 4.1: Detector Specifications.

4.1.2 Interpretting Ion Images

In a VMI ion image, the jet or droplet beam is shifted with respect to the center of the background, which is located at 0 m s^{-1}. This is because the molecular jet (or droplet beam) is travelling at 250 m s^{-1} to 1750 m s^{-1}, and so the parent ion is shifted along the direction of propagation. This is shown with the red circles in Figure 4.4 for a droplet beam. In order to experimentally measure the speed of the molecular jet or estimate the center of the droplet beam, the scaling factor for velocity can be reformulated to accommodate mass by dividing out $\sqrt{76}$, so $C = 199.56\sqrt{AMU}(m/s)/pix$. The center for CE is located at this shifted spot,

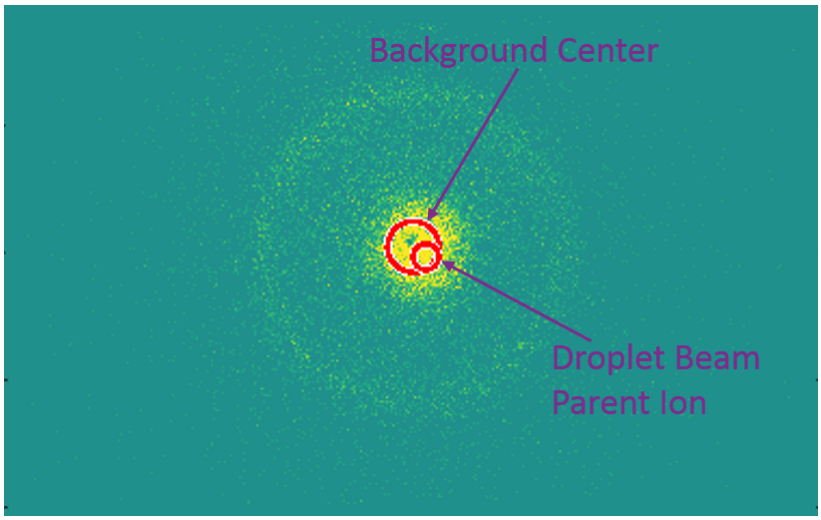

Figure 4.4: The shift of the jet with respect to the background.

where the parent ion is. In general, the larger the shift of the parent ion spot is away from the background center, the easier background subtraction is. This is because we focus on measuring the channel, which means we analyze that ions that lie in a radial range around the peak at 100 pix in the bottom right of Figure 4.3, for example. Since the background ions will be at the same radius from a different center (the background centre), the contribution of background ions will be less in this bin.

The angular dependence of the velocities allow the orientation of the molecule to be directly observed for many different ionization pathways. This is quantified by the metric, $\langle \cos^2 \theta_{2D} \rangle$, where θ_{2D} is the angle between the molecule and laser polarization axes projected onto the plane of the detector, as illustrated in Figure 4.5. When the molecules are excited by the CF, they are following it's polarization vector and are pulled into the plane of rotation, which we call planar confinement. This means that the angle the molecular axis makes with the plane of rotation goes to $0, \pi$. When the molecules are ionized without the CF and a probe that is polarized parallel to the time of flight axis, the probe is along the same direction as the plane of rotation and so the ion image has anisotropy as well.

By changing the arrival time of the probe relative to the pump pulse, the dynamical behaviour of the molecule can be studied as well. Before the CF arrives, the distribution is a ring and $\langle \cos^2 \theta_{2D} \rangle = 0.5$. As the probe moves to arrive after the CF, $\langle \cos^2 \theta_{2D} \rangle \to 1$ and this squeezing into a horizontal line is maintained long after the CF leaves.

The VMI technique is useful for understanding how the motion of the molecule

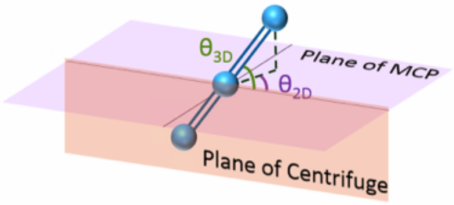

Figure 4.5: Illustration depicting the angle important in quantifying how much the molecule is squeezed into the plane of the centrifuge. For high J states, the molecule is squeezed into a line so that that $\theta_{2D} \to 0, \pi$.

changes in the helium environment and lends an easy way of studying the dissipation of rotational energy into the helium molecules since the decay of the excitation can be measured. However, because of the effusive doping gas, the background has to be taken care of. This is done using a shutter and collecting ions for a fixed time and subsequently subtracted the on and off states. As mentioned briefly above, the velocity center can also be used to discriminate against the background. For a droplet beam, this isn't the case. The parent ion signal from the cold beam is too weak to detect against the background because the mean velocity is between $250\,\mathrm{m\,s^{-1}}$ to $450\,\mathrm{m\,s^{-1}}$ which translates into 2.5-4.5 pix for Helium and 7.1-12.8 pix for S+ and is on the edge of our resolution but we should be able to distinguish the different angular features of the distributions.

4.2 Resonance Enhanced Multiphoton Ionization

The ionization signal is used to investigate the rotational spectra of molecules which is created through resonant transitions with a tunable laser and known as resonance enhanced multiphoton ionization (REMPI). This means the angular momentum state of the molecule can be directly probed, since the ion current measured is proportional to the population of the initial level and the transition probability to the excited state. This pump probe scheme is depicted in Figure 4.6. The molecules were expanded and cooled in our UHV chamber and the ion signal was detected using the VMI imaging set up.

In oxygen the (2+1)$C^3\Pi_g(v'=2) \leftarrow\leftarrow X^3\Sigma_g(v"=0)$ transition is studied because of the high ionization cross section and ability to reproduce the rotational spectrum of [24] where the line assignment is discussed in detail. The two photon energy required for this transition was scanned over the range 69 400 cm^{-1} to 71 000 cm^{-1} (279 nm to 288 nm). It was sufficient for our purposes to choose one CF truncation (rotational state) instead of scanning through these in order to develop the technique for use in droplets. Observing these rotational resonances indicated correct beam alignment, sufficient ionization intensity, and proper focusing. The power of the REMPI technique lies in it's ability to measure small signals and obtain a high degree of spectral resolution.

4.2.1 Dye Laser System

The tunable laser used to resonantly probe molecules is a Sirah Cobra Stretch pumped by a Quanta Ray 50 Hz Nd:YAG laser with a frequency doubling unit from Spectra Physics. The gain curve of the dye should match the molecule of interest; for oxygen we frequency doubled light from Rhodamine 6G. Rhodamine 6G was dissolved in ethanol with a concentration of 0.09 $\mathrm{g\,L}^{-1}$ and 0.011 25 $\mathrm{g\,L}^{-1}$ for the resonator and amplifier cells, respectively. This output was directed to a BBO crystal for second harmonic generation to deliver a wavelength range of 279 nm to 288 nm. The crystal angle was computer controlled to follow the optimal phase

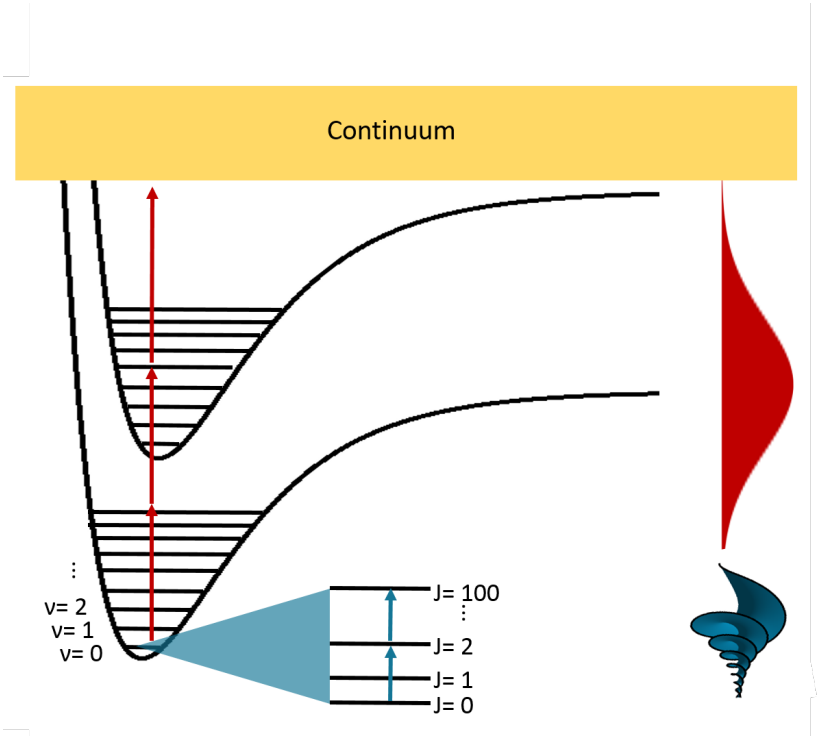

Figure 4.6: CF and (2+1)REMPI excitation scheme of Oxygen.

matched position and deliver maximum power. These pulses are ≈ 10 ns in duration and have a linewidth of 0.1 cm^{-1}. Typically, the energy delivered by the laser at 287 nm was 3 mJ per pulse. This light was directed to the UHV chamber with 4 Pellin Broca prisms in order to minimize the amount of losses to the beam and because the Al mirrors were burning. The light was directed into the chamber, and combined with the CF, using a dichroic mirror (Thorlabs DMLP900L). Typically the energy incident on the dichroic was ≈1.2 mJ, leading to an energy of about 0.7 mJ to 1 mJ going into the UHV chamber for 287 nm. If the energy going into the chamber was <500 µJ we would not be able to detect a signal.

Synchronization of the CF and the UV pulses required triggering the Nd:YAG laser with a trigger from the femtosecond laser. The Legend is equipped with a controller that can output a 50 Hz pulse synchronized with the 1 kHz output. This

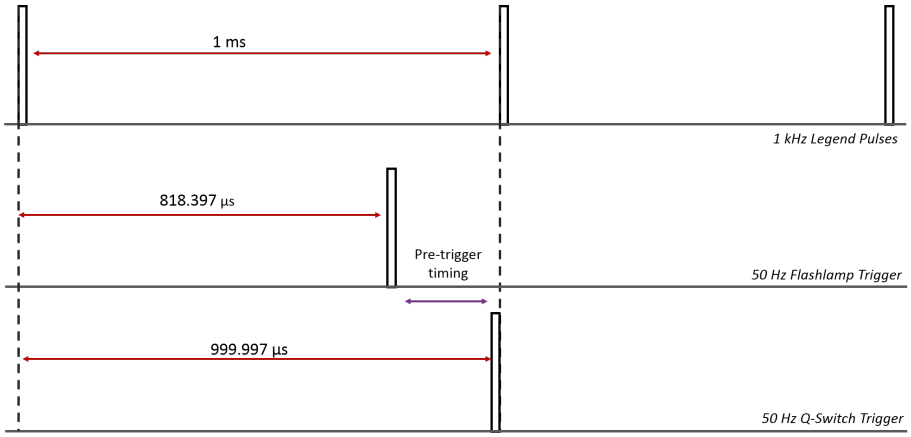

Figure 4.7: The timing diagram that shows how the YAG laser is triggered with respect to the Legend laser.

allowed the flashlamps and the Q-switch to be triggered independently by a pulse generator in order to optmize power with the CF pulses. We set the Q-switch trigger to be with "the next" expected pulse of the 1 kHz trigger signal (around 1 ms) in order to allow us to pre-trigger the flashlamps of the YAG. This couldn't be done around $t = 0$ because the delay generator did not allow negative delay times (it also meant we added 1 ms to the mass gate timing for the MCP which had a completely different calibration for the 50 Hz signal). The flashlamps were triggered $\approx$180 µs before this, and the exact position was determined by optimizing the power from the YAG. So, the Q-switch trigger was set to a delay of 999.997 µs (pulse width 5 µs) and the flash lamp trigger was set to 818.397 µs (pulse width 5 µs). The timing diagram in Figure 4.7 illustrates this scheme.

The output of Sirah is a slightly expanding beam that normally has an elongated profile vertically. Near the entrance to the UHV chamber, the beam would look like the left image in Figure 4.8. However, once this beam goes to the refocusing mirror in the chamber, it does not focus to the center of the molecular jet beam. This was deduced from spatial map imaging (SMI) mode and seeing that the UV beam was focused to a different spot than the fs beam. A telescope was installed after the first set of Pellin Broca prisms, with one lens on an adjustable rail. This

changed the angle of the beams enough to shift the focal spot of the beam in the UHV chamber. With the telescope in the beam path, when the beam is reflected from the entrance of the UHV chamber onto a wall ≈5 m away we see the spot on the right in Figure 4.8. The beam shape is far from ideal, but could be focused sufficiently to get a strong ion signal. The telescope installed in the UV beam path

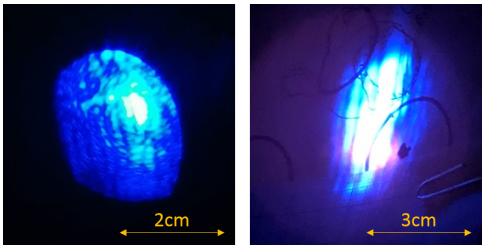

Figure 4.8: Output beam profile of the Sirah at the UHV chamber without a telescope *left* and in far field with the telescope *right*.

had the first lens with a focal length of −30 mm and the second lens had a focal length of 125 mm. They were set a distance of 13.5 cm apart. This distance was determined by aligning the fs probe and the UV probe in what's called SMI mode. This means that instead of the velocity vectors being mapped onto the detector, the ions origin position is (like normal imaging). This requires us to change the ratio of V_E/V_R from 0.718 to ≈ 0.9[42]. The mass gate on the MCP has to be extended by 100 ns to accommodate the different arrival positions based on where the ions are born. Then, if the fs probe is focused to a position that gives the optimal ionization signal from O_2+, the UV probe can be adjusted using the telescope and dichroic mirror to align with the fs probe spot. This adjusts the focus closer/further from the refocusing mirror and along/against the direction of beam propagation. How well the beams are aligned vertically could not be determined in SMI mode because the MCP gate delay had to be opened up by 100 ns in order to view both the UV and fs probe spots together. It was suspected that the difference in TOF was due to vertical misalignment but we were not able to substantially correct the timing by adjusting the beams vertically. Meanwhile, other imaging set ups actually report that a misalignment of 2 mm results in a TOF different of ≈100 ns for V_R =3000 V[16]. It is possible that this is occurring because we are not in "true SMI" mode for our set up, which could be confirmed with SIMION simulations. Additionally, our

electrodes are very small and ions that are born far away from the middle of the detector may not be properly focused which would change the expected behaviour in SMI mode. The UV probe focal spot is quite large due to the bad profile and this is certainly the case. Further investigation is required to pin down why this didn't work, but the beams were aligned without the need of this tool. The vertical alignment was done by directing the beam to the far field and adjusted the beam's vertical position and then by optimizing the ionization signal from fs probe + UV probe. Assuming the CF is aligned with the fs probe, the UV probe will be close to overlapping with the CF though this procedure only gets one close to alignment. The final vertical adjustments should be done in VMI mode looking at a particular wavelength where only rotational excitation will be observed, like 285.94 nm for the CF truncated to 10 nm/arm, until the signal is maximized.

Chapter 5

Experimental Results

5.1 Direct Measurement of Molecular Orientation

5.1.1 Kick Alignment as a Benchmark Experiment

There have been studies already conducted on impulsively aligning molecules embedded in helium nanodroplets[10][40][9][36]. While many of these molecules would be difficult to spin with the CF because they are heavy or not linear, the kick technique can still be used for rotational excitations and as a benchmark experiment to compare to the work done in droplets already. Fortunately, we can even compare with a molecule that will also spin well in the CF - CS_2. If we can measure a response in the alignment of this molecule with a kick, we will know that doping conditions are good and the droplet beam is produced sufficiently well for CF experimentation since the results are known. With kick alignment, the timescale of the excitation is important. As previously described, the helium nanodroplet can act as a bath that counteracts rotational excitation (similar to centrifugal distortion). This can also act as a sort of barrier or "rotational speed limit" for superfluidity. If the molecule can be spun fast enough to reach this barrier before the nanodroplet can equilibrate this rotational energy with phonons, the molecule "breaks free" from the helium bath and can spin without friction[10]. When measuring the molecular orientation of the molecule as quantified by $< \cos^2 \theta_{2D} >$, we would reproduce the oscillations measured in [10] whose behaviour is qualitatively shown in Figure 5.1

with respect to the free particle, or gas phase, behaviour. The oscillations have a period of about 60 ps and almost totally decay by the time the full alignment revival is expected at 152.9 ps, as calculated according to Equation 2.29. These features are entirely washed out by the helium nanodroplet interactions. It was also found that if the fluence was too high, the oscillations would die out which is different from the gas phase behaviour where the alignment would be stronger, since the number of J states populated is proportional to the fluence. This would also act as a way to calibrate the actual intensity in the interaction region and be useful to distinguish between an effusive background signal and a doped droplet signal.

It is not clear if the CF will be able to excite the molecule fast enough to allow it to spin freely. We don't know if we should look for small changes in planar confinement or if the lack of a large change indicates a problem. The idea of using both the kick alignment pulse and the CF pulse is to compare an effect that is known to the new effects excited by the CF in droplets, and therefore, in the marginal conditions of the experimental apparatus. Besides the background in the detection region, the other major hurdle is the interplay between ease of spinning a molecule with the centrifuge and the degree to which the molecular fragments will scatter with the helium droplet atoms upon Coulomb explosion. The centrifuge spins light diatomic molecules, like N_2 and O_2, very well in a molecular jet but these molecules will have their initial orientation inside the droplets lost upon Coulomb explosion. Larger, heavier molecules are also spun well by the centrifuge but can sometimes be ionized by the centrifuge alone giving rise to an anisotropic background signal, like with CS_2, for example. These molecules will maintain their initial orientation without recoil from collisions, but it can make interpreting results less clear due to that anisoptropic ionization. This forces "a race to the bottom" where the signal is lowered by making the droplets smaller, making the CF less intense, and by truncating the centrifuge so that only small changes in $\langle \cos^2 \theta_{2D} \rangle$ are expected.

The gas phase dynamics had to be reproduced in our set up before moving to nanodroplets and this was explored for the original heavy CS_2 rotor and also light rotors like N_2 and O_2 in order to extend the original study of [10]. To recover the expected behaviour of our light rotors, a $\approx$90 fs kick pulse was used because they

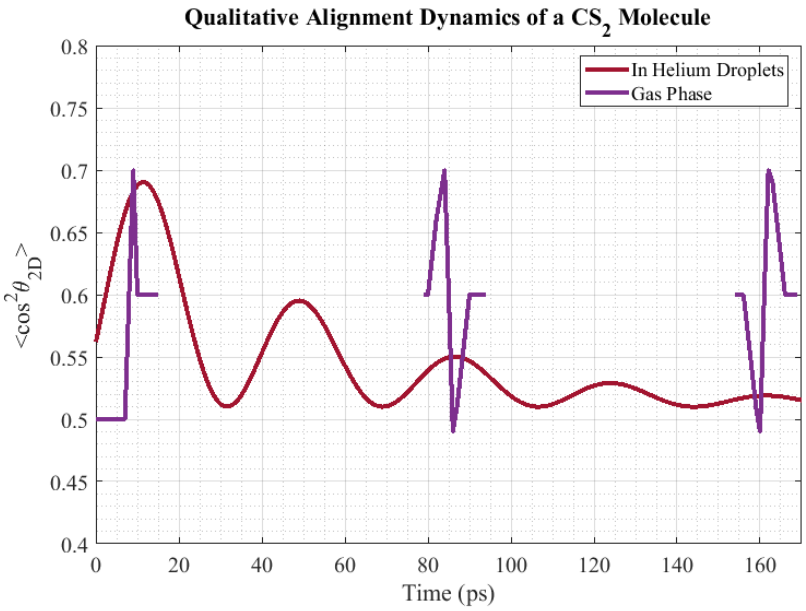

Figure 5.1: An illustrative sketch of the dynamics of CS_2 doped helium nanodroplets found in [10] in comparison to their gas phase kick dynamics found in [27]. This highlights how the helium interactions change the response of the rotor to the kick alignment pulse. The gas phase CS_2 molecules go through alignment/anti-alignment peaks and show characteristic half and full revivals at 76.5 ps and 152.9 ps, respectively, whereas the response of the CS_2 doped helium droplets look like an exponentially decaying sinusoid with a period that is less than the half revival time. The difference in the dynamics will be extremely useful in distinguishing the background (gas phase, revivals) to the signal (droplet, oscillations) response.

have a much shorter rotational period and the pulses should have a correspondingly faster rise time to be non-adiabatic. The full revivals of these molecules are 8.4 ps and 11.3 ps, respectively, which are close because of the similarity in their rotational constants. The results for N_2 are shown in Figure 5.2 in comparison to CS_2. The vertical axis has the same scale to highlight the difference in response while the horizontal axis changes to accommodate the different timescales. The absolute value of the peak alignment is expected to be closer to $\langle \cos^2 \theta_{2D} \rangle = 0.7$ for both molecules[27][32]. The alignment in CS_2 is not quite as expected, whereas the

behaviour of N_2 is very good. For the experiment with CS_2, a 300 fs pulse was used and the jet was seeded using 5 bar and 60 bar of He. The max alignment of 0.7 was achieved in the 60 bar jet and had a maximum anti-alignment dipping below 0.5 to 0.41. The 5 bar jet had a weaker response to the kick and oscillated between 0.6 and 0.48 for the alignment/anti-alignment response. The change in response observed in the left plot of Figure 5.2 is close to the response observed for the 5 bar expansion even though our experiment was done using 30 bar, which was increased from the normal 20 bar expansion and had a slight improvement. This suggests that our jet expansion is not cooling the CS_2 molecules as effectively as possible, which could be optimized by diluting the mixture further. The pulses we used were also much shorter at 90 fs and so the intensity was also very close to the ionization threshold of the molecule. In order to limit the intensity, the beam diameter could be adjusted before the refocusing lens in the vacuum chamber to make the focal volume larger, since it was about the same as the probe. When the pump beam is focused to the same size as the probe, this could lead to sampling a region not rotationally excited if the overlap is not perfect. As well, if the pump pulse is close to the intensity required to ionize the molecule this could lead to ions being created along an anisotropic polarization vector that are not actually rotationally excited - or are but cannot be distinguished. This effect is seen in the shift of $\langle \cos^2 \theta_{2D} \rangle$ before the initial alignment from 0.5 to 0.55 at $t = 0$ in CS_2.

In addition to the above, in order to try and increase the maximum alignment in CS_2 and to move towards a pulse that could be used to reproduce the oscillations in Figure 5.1, I attempted to use one arm of the centrifuge truncated to 15 ps. This pulse would have less peak intensity in the focus and would still have a sharp enough rise time with respect to the revival time (whereas it wouldn't be fast enough to kick N_2). The difference in behaviour is shown in Figure 5.3 at the full revival. The full revival is chosen to highlight field-free behavioural responses. The alignment and anti-alignment was worse for the 15 ps kick. Without ionizing the molecule more, the peak alignment could not be optimized to something more than ≈ 0.55, while 0.7 seems reasonable to expect based on the response of the molecule to similar pulses (or similar molecules to this pulse). Perhaps the alignment is small for the same reason as with the fs pulse - the molecules are not cooling efficiently

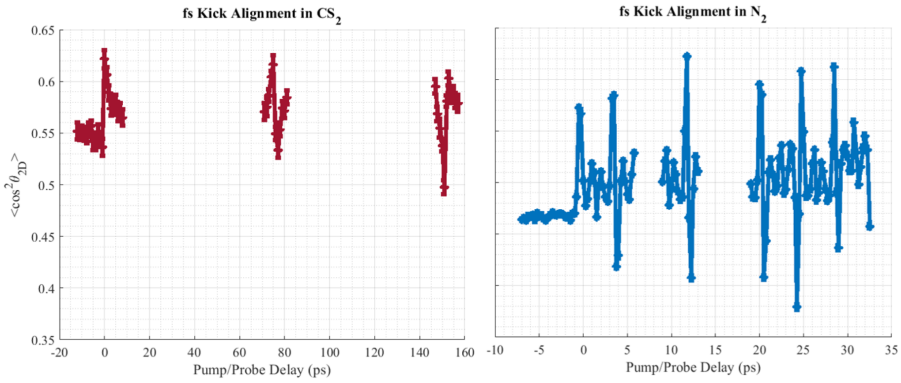

Figure 5.2: *Left:* Non adiabatic alignment of CS_2 showing the initial alignment along with the half and full revivals. This was collected from a seeded CS_2:He jet expanded from 30 bar, gating the MCP to 25 ns around S+, and the VMI set at $V_R = 4500\,\mathrm{V}$, $V_E = 3230\,\mathrm{V}$, $V_{MCP} = 815\,\mathrm{V}$ and the Phosphor Screen = 4300 V. The ions were excited by a pump pulse with a fluence of $12\,\mathrm{J\,cm^{-2}}$ ($\omega_0 = 6\,\mu\mathrm{m}$) and ionized with a probe of intensity $7.2 * 10^{14}\mathrm{W\,cm^{-2}}$ ($\omega_0 = 6\,\mu\mathrm{m}$, $\tau = 90\,\mathrm{fs}$ Gaussian pulse). *Right:* Non-adiabatic alignment of N+ showing the behaviour up to two full revivals from the initial alignment. This was collected from a pure N_2 jet expanded from 20 bar, gating the MCP to 20 ns around N+, and the VMI set at $V_R = 4500\,\mathrm{V}$, $V_E = 3230\,\mathrm{V}$, $V_{MCP} = 815\,\mathrm{V}$ and the Phosphor Screen = 4300 V. The ions were excited by a pump pulse with a fluence of $7\,\mathrm{J\,cm^{-2}}$ ($\omega_0 = 6\,\mu\mathrm{m}$) and ionized with a probe of intensity $1.2 * 10^{15}\mathrm{W\,cm^{-2}}$ ($\omega_0 = 6\,\mu\mathrm{m}$, $\tau = 90\,\mathrm{fs}$ Gaussian pulse).

in the seeded mixture because the concentration of CS_2 is too high. This, of course, wouldn't be an issue in the helium nanodroplets. It is not clear if the behaviour would be proportionally worse in droplets and that the oscillations would be much smaller because a "gentle" kick is required to see the oscillations at all.

Without a direct comparison in the gas phase experiment, it seems the best way forward is to move to the helium nanodroplet measurements. Before doing this benchmark experiment, it would be good to measure the alignment at the full revival while varying the signal to background. This means diluting the seeded gas mixture (and seeing if this indeed does improve the alignment) to a level that is about a factor of 1000 less in number density in comparison to a pure molecular beam while

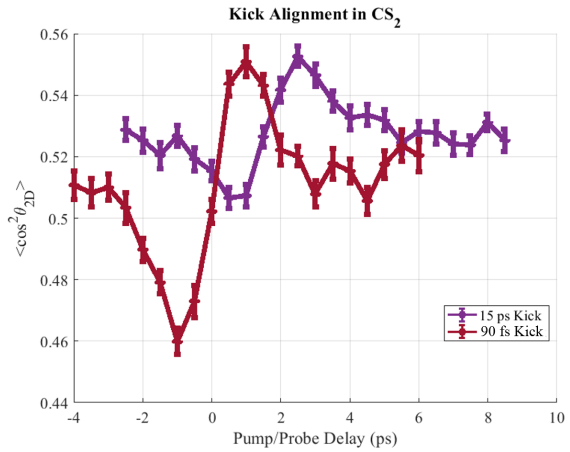

Figure 5.3: Non-adiabatic alignment of CS_2 using a 15 ps and 90 fs pulse. The collection parameters for the fs pulse are the same as in Figure 5.2. For the ps pulse, the VMI collection parameters are the same but the jet was expanded at 20 bar and the fluence was increased to $36\,\mathrm{J\,cm^{-2}}$ (ω_0 = 8 µm) to try and increase the maximum alignment. The probe intensity was set to $2.9 * 10^{15}\mathrm{W\,cm^{-2}}$.

adding background gas that is appropriate to doping a helium nanodroplet. This type of study is described in detail in Section 5.2.2 and should be repeated here to ensure the sensitivity is sufficient to extract the alignment effect from the signal to background (S:B).

5.1.2 Planar Alignment with the Optical Centrifuge

Simulation and Technique

As already discussed, the nested configuration of the vacuum chamber leads to an effusive background of the dopant gas in the detection region of the VMI system. The dopant gas pressure, and therefore background gas signal, is determined by what pressure will give singly doped droplets. This is a maximum of about 30% of all droplets, but is normally chosen to be less in order to minimize the amount of doubly and triply doped droplets. In order to determine whether or not the chosen

metric of planar confinement, $< \cos^2 \theta_{2D} >$, can be measured for some ion fragment, we need to understand the effects that the background gas has on measuring the planar confinement. In order to do that, we can study a Monte Carlo simulation of different ion images and compare the ion images measured from a O_2 jet and background gas in order to simulate the conditions that occur for helium droplets. The purpose of this study is to validate the technique and to indicate what alterations in the data collection parameters (pressure, time, etc) need to be made in order to improve the measurement. Improving the measurement means recovering a small change of $< \cos^2 \theta_{2D} >$ in a reasonable amount of time.

In order to recover the signal the "beam on" $\langle \cos^2 \theta_{2D} \rangle$ from the ion image was treated as a distribution composed of the signal and the background with some weight. Then, measuring the beam off (background) distribution, the signal contribution could be determined with the following formula:

$$\begin{aligned} \langle \cos^2 \theta_{2D} \rangle_{S+B} &= F \langle \cos^2 \theta_{2D} \rangle_S + (1-F) \langle \cos^2 \theta_{2D} \rangle_B \\ \langle \cos^2 \theta_{2D} \rangle_S &= \frac{(N_{S+B} \langle \cos^2 \theta_{2D} \rangle_{S+B} - N_B \langle \cos^2 \theta_{2D} \rangle_B)}{(N_{S+B} - N_B)} \end{aligned} \tag{5.1}$$

where F is the weight and can be described by the ratio of the number of ions of the signal or background to the total number of ions measured, N_S/N_{S+B} for example. The error bars are added to the measured variables by bootstrapping the ions (random sampling with replacement) to create different distributions of $\langle \cos^2 \theta_{2D} \rangle$. The mean and standard deviations are the estimate for the populations true mean and standard error. Reporting the error on $\langle \cos^2 \theta_{2D} \rangle_S$ is done by propagating this error according to:

$$\delta^2_{\langle \cos^2 \theta_{2D} \rangle_S} = \delta^2_{C_S} = \frac{dC_S}{dN_{S+B}}^2 \delta^2_{N_{S+B}} + \frac{dC_S}{dN_B}^2 \delta^2_{N_B} + \frac{dC_S}{dC_{S+B}}^2 \delta^2_{C_{S+B}} + \frac{dC_S}{C_B}^2 \delta^2_{C_B} \tag{5.2}$$

where $\langle \cos^2 \theta_{2D} \rangle$ has been shortened to C for readability. In general, shrinking error bars is done by collecting more data and using the central limit theorem to state that the fluctuations should go like $\sqrt{N} = \sqrt{Rt}$, where N is the number of ions detected, R is the count rate, and t is the collection time. When looking at the standard error,

we divide by this number so the error will shrink. An important assumption is that the count rate is constant and there are no large fluctuations during the collection time such that the number of ions detected can no longer be modelled as a Poissonian distribution. For this type of distribution, the mean is N, the standard deviation is $\sqrt{N}$, and it approaches a Gaussian distribution as N becomes large. This is an experimental point that helps set the collection time appropriately small for each beam on/beam off cycle.

The S:B ratio is measured by looking only at the ions that affect the measurement of $\langle \cos^2 \theta_{2D} \rangle$. This means in some radial bin that corresponds to the appropriate Coulomb channel (energy range). Assuming, in the large number limit, that the S:B ratio can be represented by the ratio of two Gaussian distributions, there cannot be any error bars calculated because that ratio is a Cauchy distribution whose moments are undefined.

The purpose of representing the data this way is to show a difference between the mean value of the signal $\langle \cos^2 \theta_{2D} \rangle$ values and the background $\langle \cos^2 \theta_{2D} \rangle$. This is why we use standard error for the error bars. To be complete in our analysis, the $p-$value should be calculated to determine whether or not the difference between the means is statistically significant at the 95% confidence interval. This was calculated by generating a null hypothesis of ions distributed isotropically in the same technique described below from a sample size of 200,000 for a one-sided tail test. The S:B was 3 ± 5 and the measured $\langle \cos^2 \theta_{2D} \rangle$ was 0.505 ± 0.058.

Ions were randomly generated in pairs to compose ion images that would be similar to a CS_2 molecule. This means that there was 6 eV of rotational energy (RE) added to 3 eV of CE energy to give the total energy (TE), where the radii distances were set according to the MCP calibration outlined in Section 4.1.1. Figure 5.4 depicts the main parameters of the simulation that were changed. The angular width is the degree of confinement but it could also have to do with ionization channel or dynamic alignment from probe. In the simulation, two ions are generated 180 deg from one another (assuming the axial recoil approximation and a linear molecule) and are chosen from around 0 deg along the x-axis based on a Gaussian with the

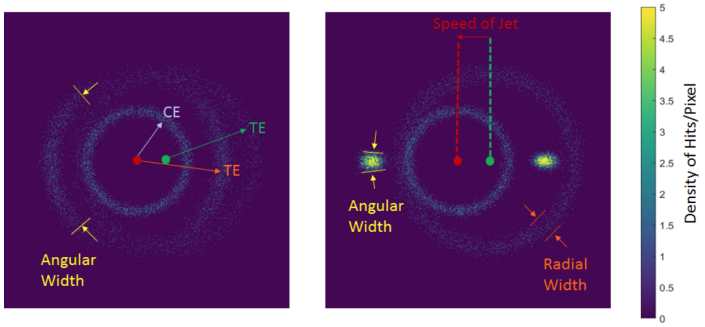

Figure 5.4: Simulating an Ion Image. The import parameters is the angular width and rotational energy of the rotating ions created. This will directly change $\langle \cos^2 \theta_{2D} \rangle$ measured. Another important parameter is the separation of the signal and the background due to the difference of velocities. Seeded jets travel at $1500\,\mathrm{m\,s^{-1}}$ and droplet beams travel at $200\,\mathrm{m\,s^{-1}}$ to $400\,\mathrm{m\,s^{-1}}$.

angular width. This is tuned to give some $\langle \cos^2 \theta_{2D} \rangle$ when there are no background ions. There is also an option to add some recoil width that randomizes where the "pair" ion is generated, but this is not considered in the following results. The radial width is chosen to represent a cross section of a few of the velocity spherical shells and the poor resolution of the raw image process. It was chosen to be a Gaussian spread since, in terms of vectorial velocity, the Boltzman distribution is Gaussian (whereas the speed is a Chi distribution). So the radial width, $R(r)$, is then randomly sampled from a distribution of the form:

$$R(r) = \frac{1}{\sigma_R \sqrt{2\pi}} e^{\frac{-(r-\mu_R)^2)}{2\sigma_R^2}} \tag{5.3}$$

where μ_R is where the radius should be based on the input energy, calculated from $\sqrt{TE/C}$, and σ_R is the channel resolution. For example, for the null distribution CE = 3 eV, RE = 3 eV, and C = $2.064 * 10^{-4}$eV/pix^2 so TE = 4.25 eV and $\mu_R = 143.64$. Although the measured experimental resolution would be ≈0.9 eV at this energy, σ_R is typically chosen to be smaller in order to decouple physical effects and the effect of the detector. For the null distribution it was set to $\sigma_R = 0.02$. The background was shifted with respect to the center of the image based on how fast the jet should

		30 h Collection Time		3 h Collection Time	
S:B	True $\langle\cos^2\theta_{2D}\rangle$	Smallest $\langle\cos^2\theta_{2D}\rangle$	p value	Smallest $\langle\cos^2\theta_{2D}\rangle$	p value
10^1	0.51	0.511 ± 0.004	0.003	0.528 ± 0.007	0.00003
10^0	0.51	0.513 ± 0.006	0.02	0.59 ± 0.04	0.01
10^{-1}	0.56	0.56 ± 0.02	0.001	0.70 ± 0.05	0.00003
10^{-2}	0.72	0.7 ± 0.1	0.02	N/A	N/A

Table 5.1: Table describing background subtraction sensitivity and collection time for 95% confidence intervals ($p < 0.05$ is significant) with respect to a null distribution of $\langle\cos^2\theta_{2D}\rangle = 0.5$.

be moving, and in this case, assumed to be an isotropic distribution. Alternatively, the distribution could have the same angular width as the signal but be shifted. The total number of ions used in the simulation is what dictates the data collection time, and was calculated assuming a (low) count rate of 3 ions per frame. This is important so that ions do not overlap for peak counting which would result in errors in the counting algorithm (saturation effects). As well, the trajectories of the particles could be distorted if there were space charge effects from multiple ions being created at the same time[50].

Table. 5.1 shows the simulated results for distributions equivalent to two different times of data collection for various S:B ratios. The smallest $\langle\cos^2\theta_{2D}\rangle$ means the significant level of the mean $\langle\cos^2\theta_{2D}\rangle$ measured for the signal is different from the null hypothesis within 95% confidence intervals. So, with $p < 0.05$, the measurement is different than an ion image with $\langle\cos^2\theta_{2D}\rangle = 0.505$. The lower the S:B, the bigger $\langle\cos^2\theta_{2D}\rangle$ has to be before the measurement is significantly different from something isotropic. When S:B is high, smaller differences can be resolved for the equivalent experimental time. Note that if N/A is the result, it means the error bars were too large to resolve any difference from the background. These results show that if we want to measure $\langle\cos^2\theta_{2D}\rangle = 0.7$, we can do so in 3 h ($\approx 3$ million ions) of data collection when the S:B is 10^{-1}. If S:B is 10^{-2}, we would need 30 h (≈ 31 million ions). The data collection time is determined using the 3 ion-

s/frame with a collection speed of ≈ 97 fps to give the total number of ions collected. The collection speed is determined by the laser repetition rate and camera frame rate.

From the simulation results of in Table. 5.1, it seems that $\langle \cos^2 \theta_{2D} \rangle$ is a good metric to measure the planar confinement in droplet like conditions. However, they still needed to be experimentally verified and this is discussed in the following section.

Experiment

In various S:B conditions, $\langle \cos^2 \theta_{2D} \rangle$ was measured in an O_2 jet using the image subtraction technique discussed in the previous section over 1 h and 3 h. The S:B was varied by adding more effusive background gas through the doping chamber to a pure molecular jet of O_2. The "true $\langle \cos^2 \theta_{2D} \rangle$" expected was 0.57 and 0.864. They were measured in the case with no added background gas over 3 h using the CF and probe.

Analyzing Figure 5.5 suggests that these techniques are successfully recovering the signal since the percent difference is less than 10% and the error bars are small. As the S:B approaches 10^{-1} the error bars grow and the mean shifts further away from the true value, though the error bars do not blow up. This would be interpreted as both techniques working to recover this signal. However, the error bars are too small to cover the systematic error. The drift of the mean value of $\langle \cos^2 \theta_{2D} \rangle$ away from the true value doesn't necessarily suggest that the background is high enough to cause an error. The probe overlap with the centrifuge can drift and actually cause a lower value of $\langle \cos^2 \theta_{2D} \rangle$ than expected. In other words, although the mean drifts from the true value measurement in "ideal conditions" as the background is increased, we may be recovering the proper $\langle \cos^2 \theta_{2D} \rangle$. In other words, the error is actually in the definition of true $\langle \cos^2 \theta_{2D} \rangle$. Since this effect didn't cause the error bars to blow up, we conclude that the drift doesn't affect the measurements over the timescale of 1.5 hours.

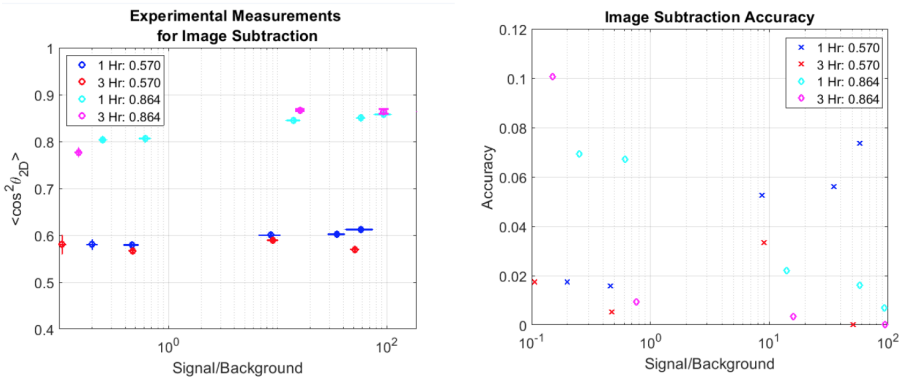

Figure 5.5: Left: The image subtraction results for 1 hour of measurements (30 minutes per pump/probe delay) and for 3 hours of measurements (1.5 hours per pump/probe delay). Right: The accuracy (or percent difference) between the measured value and the true value. 10% difference would need error bars of 0.06 and 0.09 for 0.570 and 0.864 to cover the difference of means. As well, the measurements capture the true value better for the 3 hr measurements (red and pink points) except for the 3 hr measurement with low S:B. See below for discussion.

After this confirmation of the technique, we moved to a CS_2 doped droplet beam using *only* the probe polarized perpendicular to the TOF path. This was done to decouple any effects (or lack thereof) due to rotation. These results are illustrated in Figure 5.6 and seem to be successful - we measured $\langle\cos^2\theta_{2D}\rangle = 0.651 \pm 0.005$ which is around the expected value of 0.7-0.75 (the $\langle\cos^2\theta_{2D}\rangle$ of S+ in the seeded jet using the probe). In fact, in the beam on image (containing both signal and background) $\langle\cos^2\theta_{2D}\rangle = 0.73$, and so measuring 0.651 would be an effect of scattering with the helium nanodroplets after ionization. Our ability to extract this value is in agreement with the simulations from Table 5.1 because the S:B $= 0.1 - 0.6$ and the change in $\langle\cos^2\theta_{2D}\rangle \geq 0.2$.

From this positive result, we decided to proceed to the experiments with the CF. With considerations for ionization from the CF pulse and field alignment, the CF was truncated to 30 ps. This length of CF should excite molecules to $\langle\cos^2\theta_{2D}\rangle \approx 0.6$ as measured in the seeded molecular jet with no added background, so if the helium

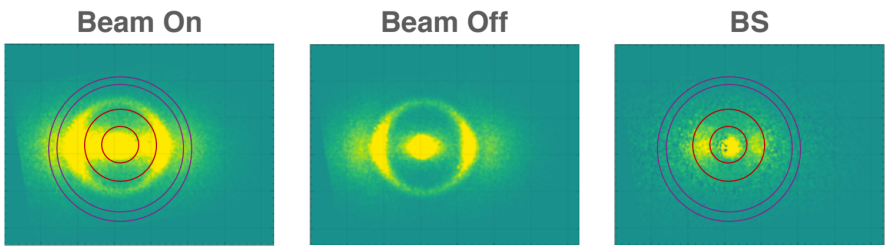

Figure 5.6: Image subtraction technique used to extract the signal. Left to right: Beam On = Doped droplets and background, Beam off = background, BS = Beam On - Beam Off. The red rings indicate the region considered for measuring $\langle \cos^2 \theta_{2D} \rangle$ and correspond to the energy range 0.5 eV to 2.5 eV, which was chosen because helium droplets shifted the kinetic energies to lower values, or the center of the image. In BS, $\langle \cos^2 \theta_{2D} \rangle = 0.651 \pm 0.005$ and in Beam On/Beam Off $\langle \cos^2 \theta_{2D} \rangle = 0.73$. In contrast, the purple rings show the typical region measured for a seeded molecular jet experiment and correspond to an energy range of 6.3 eV to 8.3 eV. There were much fewer counts in the BS image, and $\langle \cos^2 \theta_{2D} \rangle = 0.66 \pm 0.03$.

interactions are strong the signal will have $\langle \cos^2 \theta_{2D} \rangle < 0.6$. Based on the simulation and experimental verification of the technique so far, we would expect ≈3 h of data collection be enough to resolve the effect.

The measurement is shown in Figure 5.8 with the CF working and the CF broken for beam on (with droplets) and beam off (no droplets) measurements on the left, and the signal calculations on the right. The signal calculations are very promising and look like a result that indicates some rotation. The top panel shows the behaviour of $\langle \cos^2 \theta_{2D} \rangle$ for the warm background gas with the CF working and the CF broken. When the CF is broken, there is no planar confinement and with the CF working $\langle \cos^2 \theta_{2D} \rangle \approx 0.6$. On the bottom panel, the signal in droplets is plotted. The broken CF gives some alignment effect that decays away after the pulse is gone, as does the working CF. The working CF has strong planar confinement that lasts about 10 ps longer than the broken CF. This would be expected if we did not rotate the molecules fast enough and the alignment decayed away. From the plot on the left, we can conclude that we are successfully measuring an anisotropic effect in

the signal that is statistically different from the background, at least during the CF excitation pulse. However, we do not know if this is just an effect of alignment since the behaviour between the broken CF and working CF are so similar.

The problem with interpreting these results is that the broken CF excites an

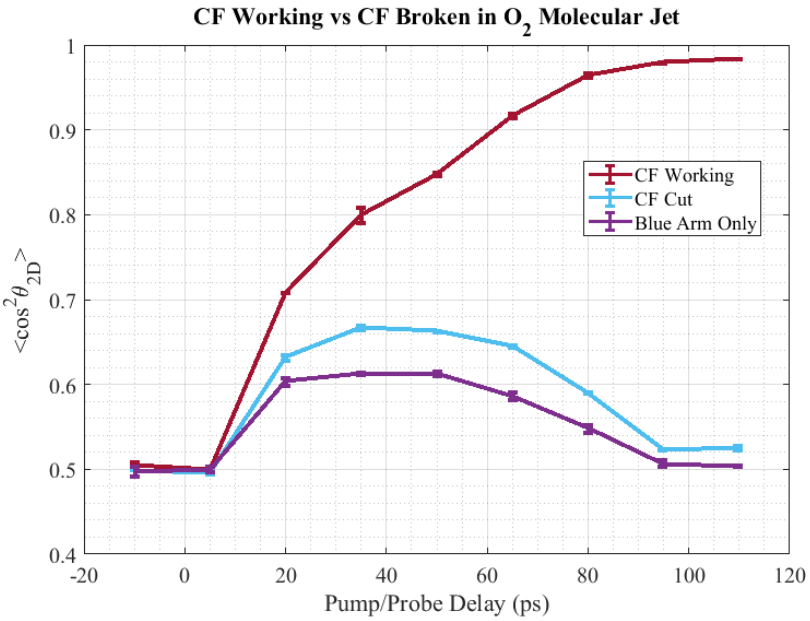

Figure 5.7: Example of the anisotropic effect that the broken CF has in comparison to the working CF in a molecular jet experiment of O_2 expanded at 20 bar. In molecular jet experiments, we know that the CF is working to spin molecules because there is a lasting effect past ≈100 ps, but at the beginning between 0 ps to 20 ps it is difficult to distinguish. Collected with the full, untruncated CF set to $1.3 * 10^{13} \mathrm{W\,cm^{-2}}$ (average energy 2.1 mJ) and the probe set to $2.3 * 10^{15} \mathrm{W\,cm^{-2}}$ and VMI settings for O+ at V_R =4500 V.

anisotropic effect during the pulse, as shown between 20 ps to 80 ps in Figure 5.7, which means that we cannot directly conclude that CS_2 is rotating because this could be an effect of alignment. The strongest response in alignment is when the field is present, and we do not know if we can resolve the decay accurately for these time steps. In the previous study in Figure 5.6 we were only looking at an

alignment effect and our verification technique was only tested to distinguish against an isotropic signal (no effect). The technique has not been characterized in a way that we know we can reliably distinguish against two similar anisotropic signals. Outside of droplets in the molecular jet experiments the broken CF can elicit the same type of response in CS_2 or O_2 that is typical of adiabatic alignment pulses, where the molecules are aligned while the field is present[27], though the pulse is short and more like a kick, but there are no revivals. The circularly polarized light rotates too quickly for the molecules to follow but the molecules are still pulled to the rotational plane, as shown in Figure 5.7. We distinguish against this "alignment" effect by observing the lasting planar confinement, which can be seen by looking at the lasting effect that is observed in the background signal on the left of Figure 5.8 and clearly in Figure 5.7. We cannot do the same test in droplets though.

There are some problems with the error bars in the signal calculation because they can get quite large when contribution above the background count is small (essentially dividing by zero). When the signal is stable, they are as shown in Figure 5.8, and are found via bootstrap sampling. This can make the broken CF give a higher degree of anisotropy than the working CF that is statistically significant. An example of this is shown in Figure 5.9. The curves plotted are $\langle\cos^2\theta_{2D}\rangle_{workingCF} - \langle\cos^2\theta_{2D}\rangle_{brokenCF}$. In the plot on the left, the variation between 2 different runs on the same day are shown, along with the data consolidated into one run. In the plot on the right, the day to day variation is plotted. When $\Delta\langle\cos^2\theta_{2D}\rangle > 0$ this means the working CF has achieved more planar confinement or excited a more anisotropic signal than the broken CF. These plots highlight the variance of the measurements whereas the error bars plotted are the standard error and represent the statistical error in the average of the mean. The error bars do not cover the spread of the data and it seems that for reliability purposes, systematic error should be accounted for in order to diagnose operational problems. This could include accounting for changes in the doping chamber pressure or laser energy changes. As a note, the problem of the broken CF giving a higher $\langle\cos^2\theta_{2D}\rangle$ was more prevalent in 20 ps and 10 ps CF which are not shown here, whereas the 30 ps CF worked quite well.

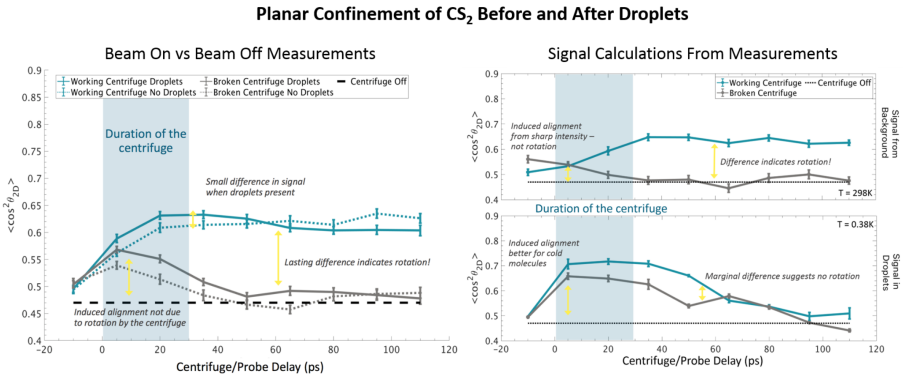

Figure 5.8: Droplet Measurements with Centrifuge. The difference in the droplet vs no droplet curves agrees with the conclusion from Figure 5.6 - we are successfully extracting a signal. However, if the signal disappears we wouldn't be sensitive to this in these measurements. These experiments were done for droplet conditions of T_N =15 K and P_0 =24 bar. The doping was set so that the CS_2+ signal counted 2 ions/frame with a probe polarized perpendicular to the TOF axis with an intensity of $2.9 * 10^{15}$ W cm^{-2}(the ion gauge was broken). The CF was set to the 6 nm/arm settings from Table 2.2 with an average energy of 0.5 mJ. The probe was polarized parallel to the TOF axis and had an intensity of $2.9 * 10^{15}$ W cm^{-2}. The VMI settings were V_R = 4500 V, V_E = 3230 V, V_{MCP} = 850 V and the Phosphor Screen = 4300 V.

In order to shrink the error bars data would have to be collected for longer, in line with the results from the simulation. In order to simulate more collection time, it is typical to use bootstrap sampling which we employed. However, that only works if the system is behaving well and implementing this strategy was difficult because of drifts and fluctuations in the system. The error bars may underestimate the true fluctuations of the system. We thought this was the case because we could not reproduce the results of Figure 5.8 reliably. Maintaining a steady doping chamber pressure was problematic because of the long line leading up to the back of the skimmer and because CS_2 is a liquid, meaning we rely on the vapour pressure filling up the line and being constant. We tried to stabilize this by placing the small vial of CS_2 connected to the system into a water bath so that room temperature fluctuations have a smaller effect. This source is also being constantly consumed,

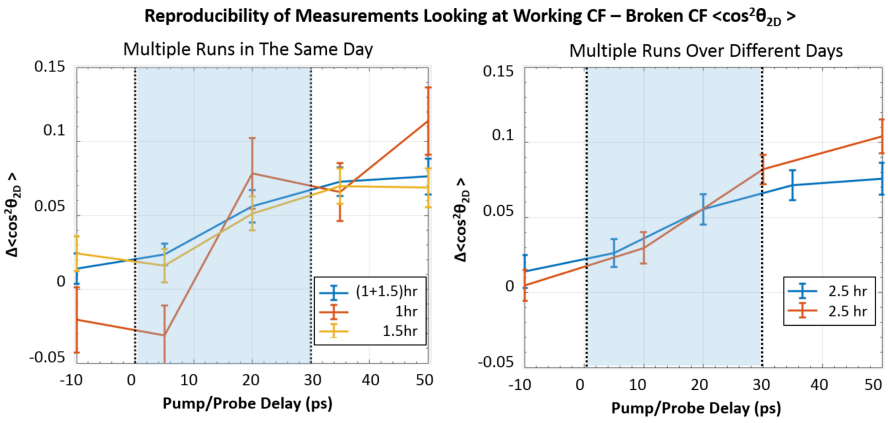

Figure 5.9: A dissection of the results plotted in Figure 5.8 for the 30 ps CF. *Left:* Variance of the data in one day over subsequent data collection runs. *Right:* Variance of the data day to day.

which means the experiment needs to be stopped at some point in order to proceed. We collect in such a way that the fluctuations can be "tracked" by the beam on/beam off subtraction and we know that we are doing a good job of this if the ion count rate has error bars that can be described by a Poissonian distribution ($\sqrt{\lambda}$). These effects were attempted to be minimized by increasing the diameter of the tubing (to prevent condensation and pressure pockets), which seemed to stabilize the partial pressure of the CS_2 signal over the course of an hour, according to the RGA measurements done in the Science Chamber with the doping chamber filled. However, this doesn't change what happens to the signal when the doping chamber pressure changes even a small amount - if it increases then the droplets can pick up more molecules and this can destroy planar confinement or if it decreases than the signal disappears altogether. The doping chamber fluctuations could not be tracked at the time of these measurements externally because the ion gauge was broken. At the same time, the CF and probe alignment drifts, seemingly as the mirrors heat up, and the experiment needs to be stopped to adjust this as well. This is difficult to exactly reproduce the same alignment since the background gas pressure is increased so the room temperature planar confinement can be optimized. This effect is difficult to see and then the system needs time to relax into steady state after this change but it would also be challenging and expensive to build a feed back system that could

maintain the beam alignment.

From the results of Figure 5.8, we can conclude that the technique for isolating the signal with respect to the background is working. We are measuring something statistically different than the background. However, we cannot drawn conclusions from the measurements regarding whether or not the molecules are rotating yet since the effect must be small in comparison to the broken CF. More understanding of the broken CF behaviour is needed in order to use this as a method to discriminate against rotation. An intermediate study, before returning to droplets, could be performed on a diluted jet using the broken CF and the working CF but truncated to a different duration. If the broken CF behaves like a circularly polarized kick, the different dynamics should be clear on shorter timescales and this would allow us to discriminate between rotation and alignment. This study would then need to be repeated in the low S:B limits expected in the droplet experience to confirm that the behaviour can be detected with our sensitivity. We may be at the limit of our detection sensitivity, but the results are promising!

5.2 Direct Measurement of Angular Momenta

5.2.1 Resonance Enhanced Multiphoton Ionization Spectroscopy of Centrifuged Oxygen

The REMPI spectrum of oxygen excited by the centrifuge has previously been investigated by our group[24]. This technique used the CF to rotationally excite the molecule and then use a resonant probe to excite a transition between the ground state, $X^3\Sigma_g^-$, and the excited state $C^3\Pi_g$. This is typically called a (2+1) REMPI process because 2 photons are used to excited the intermediate state $C^3\Pi_g$ and another photon is needed to ionized. A diatomic the term symbol characterizes the electron spin and orbital angular momentum and is written as ${}^{2S+1}\Lambda_\Omega$, where Λ is the projection of angular momentum on the molecular axis, S is the total electronic spin angular momentum, and $\Omega = \Sigma + \Lambda$ which is the sum of the projections of electron spin (Σ) and orbital angular momentum. In a simple rigid rotor, where only

the rotational structure is important because $\Lambda = 0$ and $S = 0$, the spectra is much easier to interpret because the peaks correspond to rotational transitions. Oxygen is more complicated because the ground state has $\Lambda = 0$ and $S \neq 0$ and follows Hund's b rule. This means the ground state is a triplet and that for each of these levels there are 3 possible J states. The excited state has $\Lambda = 1$ and $S \neq 0$ and follows Hund's a rule. This means there are, again, three different sets of J states for each $\Omega = 0, 1, 2$. The CF was used to control the rotational excitation of oxygen already for levels between 0 and ≈ 120.

By truncating the spectrum of the CF, accurate control of the final rotational state is possible. In order to fit the excitations of each branch from the ground state, the CF truncation can be scanned along with the photon energy of the nanosecond probe used to resonantly ionize the excited oxygen and the ions peaks can be fit to the expected Fortrat. A 2D REMPI spectrogram was measured and analyzed in [24] and was the guide for our preliminary studies. One CF truncation scan is shown in Figure 5.10 in comparison to the nanosecond probe only. The horizontal axis is the energy of the 2 photons used to excited the intermediate oxygen state converted from the laser wavelength and the vertical axis is just the normalized intensity, with the scans shifted in order to show the differences. The 6 nm/arm CF should be able to rotate molecules to $J \approx 33$, and one of the branches has a $J = 34$ transitions at $69\,976.56\,\mathrm{cm}^{-1}$. The scan with no CF and just the nanosecond probe showed that the molecular jet has a temperature of 10 K and has a maximum rotational state of $J = 6$, which is located at $69\,620\,\mathrm{cm}^{-1}$. The location of these J states are marked in Figure 5.10. When the laser wavelength is resonant with one of these transitions, an ion signal can be measured. Seeing peaks between $69\,600\,\mathrm{cm}^{-1}$ to $70\,000\,\mathrm{cm}^{-1}$ indicates that the CF is working and we are populating rotational states between $J \approx 20$ and 40. The clear difference in the two plots is a result of the CF working and redistributing the initial ground state population to higher J states in the triplet branches. These results were reproduced to have ensure that the detection and alignment were working and to allow us to chose strong transitions that could be used to study in helium nanodroplets.

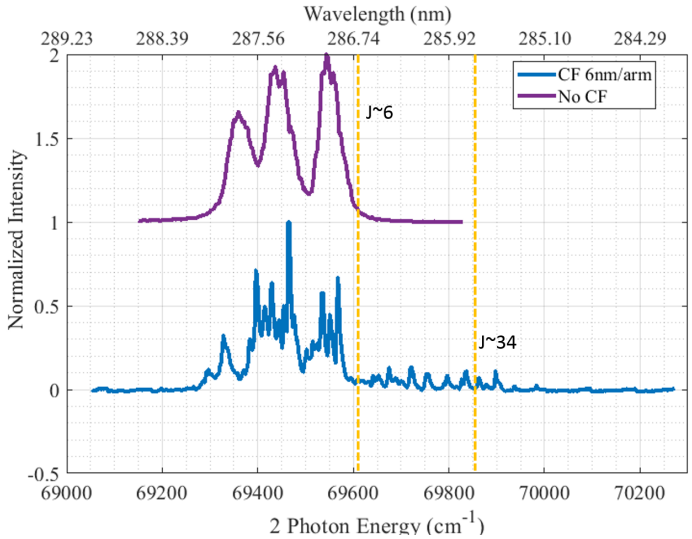

Figure 5.10: Reproducing a slice of the 2D Spectrogram in [24]. The ion signal was measured as a function of the nanosecond probe wavelength for the CF truncated to 6 nm/arm and without the CF. These scans were measured with an average energy of the nanosecond probe set to 500 µJ at 287 nm and the average energy of the CF was 0.76 mJ. The MCP was gated for O+ signal was collected with 100 averages of images taken with 30 ms of exposure time. V_R = 4500 V, V_E = 3230 V, V_{MCP} = 800 V and the Phosphor Screen = 4300 V.

5.2.2 Measurements Limiting the Signal to Background Ratio

Using the predictions made for the doped helium beam density, oxygen was diluted with helium down to about a factor of 1000x less than in a pure jet. We did this in order to determine if our detection technique was sensitive enough to recover the low count rate in the high background using both the CF and probe to study a rotationally excited state and using just the nanosecond probe to study the dependence decoupled from effects due to rotation.

There are few ways to beat the background when processing an ion image: choose a rotational state that can only be excited by the CF (not thermally) and observe the pixels in the ion image that correspond to the jet velocities or count long enough

to avoid the noise from image subtraction (and collect beam on/off). Because the helium droplets move slower than a supersonic jet; at $200\,\mathrm{m\,s^{-1}}$ to $400\,\mathrm{m\,s^{-1}}$ depending on the expansion conditions, we cannot set a crop that would only correspond to the jet based on the velocity because of the background. The most probable velocity according to the Maxwell Boltzmann distribution is given by:

$$v_{mp} = \sqrt{\frac{2k_B T}{M}} \tag{5.4}$$

where M is the mass in kilogram and T is the temperature of the reservoir in kelvin. For oxygen, $v_{mp} = 393\,\mathrm{m\,s^{-1}}$. This means that the jet spot, easily identifiable in a molecular jet experiment, will lie within the background spot and be impossible to reliably identify. So, we cannot use velocity to discriminate against the background, but it may be possible to discriminate against the background using rotational excitation.

Figure 5.11 shows the triplet branch of the ground state in oxygen, cold from expansion in a molecular jet, in comparison to warm effusive gas leaked into the science chamber. The cold jet was measured using the normal 20 bar expansion through the nozzle at room temperature and the warm distribution was measured by blocking the jet and leaking in a lot of gas into the doping chamber so that the science chamber increase was $3.32 * 10^{-7}$torr. The spectra are much different because at room temperature, when higher rotational states are populated, the bandhead in O_2 becomes apparent. The bandhead exists because the rotational constant is different for excited states ($B \rightarrow B_v$) and the spectral lines bunch together. This means the spacing is not linear and that the next J state may actually be lower in energy [19]. This is why the spectra from the warm sample looks only a little bit broader than the spectra from the jet although many more rotational states are populated.

Ideally, the CF would excite the molecules to $J > 21$. Because the molecules starts out cold and in the ground rotational state, more of them will be captured by the CF in comparison to the molecules rotating $10 < J < 21$, for example. Not a lot of this population will be transferred to higher J states by the CF and so the

ion signal will be much less there. The molecular jet is 10 K whereas the inside of helium nanodroplets will be 0.4 K.

In molecular jet experiments, it was very useful to use wavelength and rotation to

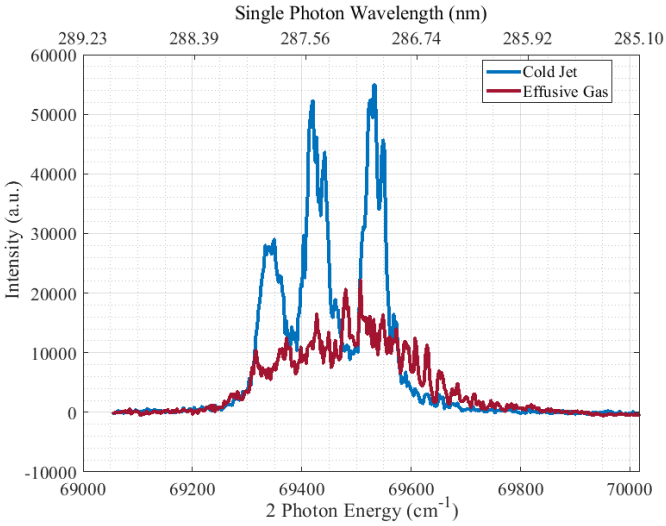

Figure 5.11: Cold Oxygen, 10 K in blue, vs Warm Oxygen, 298 K in red. Ionization signal from the nanosecond probe only set to an energy of 500 µJ at 287 nm. The cold distribution is from 20 bar expansion of pure O_2 and the warm distribution is from adding $3.32 * 10^{-7}$torr O_2 to the science chamber via the doping chamber. V_R = 4500 V, V_E = 3230 V, V_{MCP} = 1000 V and the Phosphor Screen = 4300 V.

discriminate against the background. Moderately truncating the CF and observing a J state that cannot be reached through thermal excitation (or background excitation) allowed us to observe a noise free signal when the jet density was reduced by a factor of 0.039. These results are shown in Figure 5.12 for a molecule excited by the 7 nm/arm CF ($\approx 38\hbar$ truncation) and the diluted O_2 jet had no background gas added. The signal is diluted by adding more Helium gas and the dilution level is compared to a pure jet of oxygen. The ion signal is recorded using peak counting, so the noise level is low and $\approx$ 1 ion over the course of the measurement. This experiment was only done for a dilution level of 0.039, whereas a level of 0.0053

is the dilution level expected to compare to a droplet experiment. As well, this technique relies on our ability to actually rotate molecules that are embedded in helium and we don't know if this will happen yet (or if it will be excited to the same J state). However, this served as a good preliminary study since the sensitivity can be increased by increasing the collection time without increasing the noise. This means we can detect a background free CF signal that is 100x less dense than the molecular jet and it has the potential to be pushed further to observing a signal that is 1000x less dense like in the droplet experiment.

In the worse case scenario, the molecules will not be rotating in a superfluid

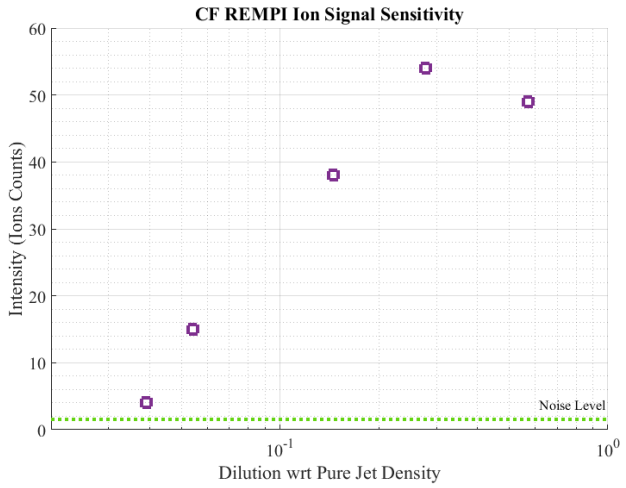

Figure 5.12: A peak counting experiment observing the ion signal the CF+probe truncated to 7 nm/arm ($\approx 38\hbar$) as a function of decreasing O_2 density and the probe was set to λ =285.26 nm. A total of 1500 frames (at 50 Hz, ¡1 min of collection time) were collected for each data point and the MCP was gated to observe the O_2+. V_R = 4500 V, V_E = 3230 V, V_{MCP} = 800 V and the Phosphor Screen = 4300 V. The diluted gas was expanded through the nozzle at room temperature with P_0=20 bar.

environment and so the CF will not be able to excite the high rotational levels that are easily distinguishable from the warm background. This means studying resonant peaks that are within the warm distribution of Figure 5.11 instead of outside of

it. In order to recover this signal, we will have to rely on our ability to increase measurement time and do background subtraction. Towards this direction, 5 measurements were taken at wavelengths near the middle triplet peak of oxygen. These are shown in Figure 5.13. At the transition corresponding to a two photon energy of 69 420 cm^{-1} in the middle of the triplet (the $J' = 2 \leftarrow J = 0$ transition of the F_2 branch for $N = 1$), a pure molecular jet of oxygen (signal dilution = $n/n_{MJ} = 1$) has $\approx 10^4$ counts in 10,000 frames, or 3.5 min of collection time. As the signal density was lowered by an order of magnitude, the ion signal also decreased by about an order of magnitude. When a dilution was reached that was equivalent to the number density expected in the helium nanodroplet experiment, effusive background gas was added to simulate dimer doping (the purple dot). The error bars added are the 1 standard deviation value between 5 different measurements. When the beam is blocked and the effusive background gas is still there, we measure the blue dotted line which is plotted to show the difference between beam on and beam off. With these few statistics, we can see that there is a clear difference between beam on and beam off and we can tentatively conclude that we are successfully measuring the O_2+ signal from the doped droplets since the ion signal from the effusive background is negligible.

This technique is confirmed to be working in the molecular jet but at the time of this thesis, no signal was recovered in nanodroplets. This could indicate that the droplet density is much lower than expected. This could be the case if the droplets with 5000 atoms are not forming, which we assume in the density calculations. If the beam is less dense than expected, a different detection technique should be employed because it is near it's limit of sensitivity. However, the collection time should be increased and the doping pressure can be increased to verify the presence of some signal to diagnose this problem but was not pursued here. Regardless, the sensitivity of the REMPI technique has been demonstrated to be capable of recovering an O_2+ ion signal that is 1000x less dense than what is measured in a pure molecular jet from a background ion signal that is comparable to what is present when doubly doping helium nanodroplets.

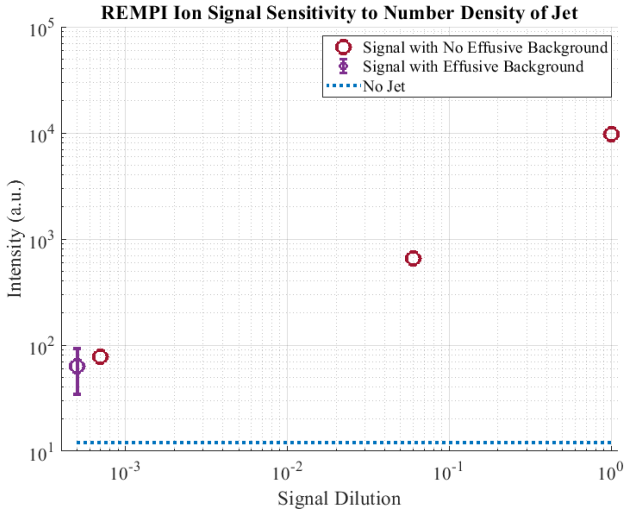

Figure 5.13: Using the nanosecond probe only, the transitions were investigated by lowering the signal density and added background gas. Our detection set up was sensitive enough to capture a small signal 0.0007 times lower than a pure molecular jet.

Chapter 6

Conclusion

In this work, techniques were developed that would allow the rotational excitation of molecules in helium nanodroplets to be studied using an optical centrifuge. The detection limitations in this unique droplet machine were characterized and addressing these limitations will be the first step in pushing the project forward.

Two different experimental techniques were proposed: direct measurement of molecular orientation and direct measurement of angular momenta. These were explored for two different rotors (heavy and light) that are expected to have a different type of interaction with the helium environment. For the molecular orientation technique that used VMI, the $\langle \cos^2 \theta_{2D} \rangle$ signal was measured down to a S:B ratio of 10^{-1} and successfully recovered $\langle \cos^2 \theta_{2D} \rangle = 0.57$. When the S:B reaches 10^{-2} problems start to occur in the signal recovery and we are only sensitive to larger changes in $\langle \cos^2 \theta_{2D} \rangle$. Using this technique, a CF pulse that had a value of $\langle \cos^2 \theta_{2D} \rangle = 0.6$ in a CS_2 molecular jet was applied to CS_2 doped helium nanodroplets, but no lasting rotation was observed. For the angular momenta technique that used REMPI, the ion signal was measured in a seeded jet of O_2 for one of the ground state triplet transitions. The O_2+ signal from this transition range was measured while the jet was diluted with more helium to 0.0007x the pure O_2 jet, whereas a decrease in number density to the droplet experiment is 0.0053x.

This work explored different options to study superfluidity and proposes an outline

for the future investigation. This means using two different "calibration" or "benchmark" experiments that we realized are crucial to interpreting results.

The first experiment to implement and understand is the kicked rotor in helium nanodroplets. This is the most efficient experiment to start with because it ensures that an appropriate operating point of the droplet machine can be achieved that will reproduce the results from conventional droplet machines. Chamber modifications may need to be made and these are time consuming because of the pump down time required to eliminate background gases. This gives proof that the system is stable enough to measure over the time needed to recover the signal. It will also demonstrate any discrepancies that may result due to the set up since it can be directly compared to understood physical behaviour.

The second experiment that needs to be performed is the calibration of the broken CF using REMPI spectroscopy. This allows an in-situ characterization and correlation between the J state measured (or depleted) and $\langle \cos^2 \theta_{2D} \rangle$ which we only had access to indirectly before (through Raman in a different gas chamber). This will allow us to discriminate more confidently against rotation with the broken CF, since there are some alignment effects during the field, and could ultimately allow the decay of rotational excitation to be characterized. This can be done in a seeded gas jet initially and will directly give the dependence of $\langle \cos^2 \theta_{2D} \rangle$ on the excited J states (rotational wavepacket).

In conclusion, we are producing some droplets despite the unconventional vacuum system. Some preliminary measurements have been done, but more sensitive tests are required to understand the superfluid nature inside the nanodroplets.

Bibliography

[1] E. Andronikashvili. A direct observation of two kinds of motion in helium ii. *Journal of Physics, USSR*, 10:201, 1946. → page 1

[2] P. Atkins and R. Friedman. *Molecular Quantum Mechanics*. Oxford University Press, 5th edition, 2011. → page 4

[3] C. A. Balanis. *Antenna theory: analysis and design*. Wiley, 4th edition, 2016. → page 8

[4] M. Bitter. *Quantum coherent control of laser-kicked molecular rotors*. PhD thesis, The University of British Columbia, 2016. → pages 8, 10, 14

[5] N. B. Brauer, S. Smolarek, E. Loginov, D. Mateo, A. Hernando, M. Pi, M. Barranco, W. J. Buma, and M. Drabbels. Critical Landau velocity in helium nanodroplets. *Physical Review Letters*, 111, 2013. doi:10.1103/PhysRevLett.111.153002. → page 3

[6] A. Braun. *Photodissociation studies of CH3I and CF3I in fluid 4Helium Nanodroplets*. PhD thesis, Ecole Polytechnique Federale de Lausanne, 2004. → pages 45, 46, 47, 49

[7] H. Buchenau, E. L. Knuth, J. Northby, J. P. Toennies, and C. Winkler. Mass spectra and time-of-flight distributions of helium cluster beams. *The Journal of Chemical Physics*, 92, 1990. doi:10.1063/1.458275. → page 21

[8] O. Bünermann. *Spektroskopie von Alkali- und Erdalkaliatomen, - molekülen, Alkaliclustern und Komplexen organischer Moleküle auf Heliumnanotröpfchen*. PhD thesis, Universität Bielefeld, 2006. → pages x, 37, 38

[9] A. S. Chatterley, C. Schouder, L. Christiansen, B. Shepperson, M. H. Rasmussen, and H. Stapelfeldt. Long-lasting field-free alignment of large

molecules inside helium nanodroplets. *Nature Communications*, 10, 2019. doi:10.1038/s41467-018-07995-0. → page 59

[10] I. N. Cherepanov, G. Bighin, L. Christiansen, A. V. Jørgensen, R. Schmidt, H. Stapelfeldt, and M. Lemeshko. Far-from-equilibrium dynamics of angular momentum in a quantum many-particle system. *arXiv:1906.12238*, 2019. → pages xii, 2, 59, 60, 61

[11] L. Christensen, L. Christiansen, B. Shepperson, and H. Stapelfeldt. Deconvoluting nonaxial recoil in coulomb explosion measurements of molecular axis alignment. *Phys. Rev. A*, 94, 2016. doi:10.1103/PhysRevA.94.023410. → page 44

[12] C. Ellert, H. Stapelfeldt, E. Constant, H. Sakai, J. Wright, D. M. Rayner, and P. B. Corkum. Observing molecular dynamics with timed coulomb explosion imaging. *Philosophical Transactions of the Royal Society A: Mathematical, Physical and Engineering Sciences*, 356, 1998. doi:10.1098/rsta.1998.0168. → page 44

[13] A. T. J. B. Eppink and D. H. Parker. Velocity map imaging of ions and electrons using electrostatic lenses: Application in photoelectron and photofragment ion imaging of molecular oxygen. *Review of Scientific Instruments*, 68, 1997. doi:10.1063/1.1148310. → pages 44, 45

[14] B. Friedrich and D. Herschbach. Alignment and trapping of molecules in intense laser fields. *Phys. Rev. Lett.*, 74:4623–4626, Jun 1995. doi:10.1103/PhysRevLett.74.4623. → page 10

[15] R. Fröchtenicht, J. Toennies, and A. Vilesov. High-resolution infrared spectroscopy of SF_6 embedded in he clusters. *Chemical Physics Letters*, 229, 1994. doi:https://doi.org/10.1016/0009-2614(94)01026-9. → page 1

[16] M. A. M. García. Optimization of voltages for spatial map imaging and velocity map imaging. Master's thesis, Center for Free-Electron Laser Science, 2017. → page 57

[17] S. Grebenev, J. P. Toennies, and A. F. Vilesov. Superfluidity within a small helium-4 cluster: The microscopic andronikashvili experiment. *Science*, 279, 1998. ISSN 0036-8075. doi:10.1126/science.279.5359.2083. → page 1

[18] O. F. Hagena and W. Obert. Cluster formation in expanding supersonic jets: Effect of pressure, temperature, nozzle size, and test gas. *The Journal of Chemical Physics*, 56(5), 1972. → page 21

[19] R. Hanson, R. Spearrin, and C. Goldenstein. *Diatomic Molecular Spectra*, pages 9–49. 01 2016. ISBN 978-3-319-23251-5. doi:10.1007/978-3-319-23252-2_2. → page 79

[20] A. Heidenreich, D. Schomas, and M. Mudrich. Dopant-induced ignition of helium nanoplasmas—a mechanistic study. *Journal of Physics B: Atomic, Molecular and Optical Physics*, 50, 2017. doi:10.1088/1361-6455/aa92da. → page 38

[21] F. D. Jan Harms, J. Peter Toennies. Density of superfluid helium droplets. *Physical Review B*, 58(6), 1998. → page 21

[22] J. Karczmarek, J. Wright, P. Corkum, and M. Ivanov. Optical Centrifuge for Molecules. *Physical Review Letters*, 82, 1999. doi:10.1103/PhysRevLett.82.3420. → pages 2, 14

[23] A. Korobenko. *Control of molecular rotation with an optical centrifuge*. PhD thesis, The University of British Columbia, 2016. → pages ix, 14, 15

[24] A. Korobenko, A. A. Milner, J. W. Hepburn, and V. Milner. Rotational spectroscopy with an optical centrifuge. *Phys. Chem. Chem. Phys.*, 16, 2014. doi:10.1039/C3CP54598A. → pages xv, 54, 76, 77, 78

[25] S. A. Krasnokutski and F. Huisken. Low-temperature chemistry in helium droplets: Reactions of aluminum atoms with o2 and h2o. *The Journal of Physical Chemistry A*, 115, 2011. doi:10.1021/jp112423v. → page 1

[26] S. Kregel, G. Thurston, J. Zhou, and E. Garand. A multi-plate velocity-map imaging design for high-resolution photoelectron spectroscopy. *The Journal of Chemical Physics*, 147:094201, 09 2017. doi:10.1063/1.4996011. → page 51

[27] V. Kumarappan, S. S. Viftrup, L. Holmegaard, C. Z. Bisgaard, and H. Stapelfeldt. Aligning molecules with long or short laser pulses. *Physica Scripta*, 76, 2007. doi:10.1088/0031-8949/76/3/n09. → pages xii, 61, 73

[28] Y. Kwon, P. Huang, M. V. Patel, D. Blume, and K. Whaley. Quantum solvation and molecular rotations in superfluid helium clusters. *The Journal of Chemical Physics*, 2000. → page 2

[29] M. Lemeshko. Quasiparticle approach to molecules interacting with quantum solvents. *Phys. Rev. Lett.*, 118, 2017. doi:10.1103/PhysRevLett.118.095301. → page 2

[30] M. Lemeshko and R. Schmidt. *Molecular impurities interacting with a many-particle environment: from ultracold gases to helium nanodroplets*, page Low Energy and Low Temperature Molecular Scattering. 2016. doi:10.1039/9781782626800-00444. → page 2

[31] I. MacPhail-Bartley, A. Milner, W. Wasserman, and V. Milner. Laser control of molecular rotation: Expanding the utility of an optical centrifuge. 12 2019. → pages ix, 3, 9, 10, 14, 15, 17

[32] M. Meckel. *Strong-Field Ionization of Aligned Oxygen*. PhD thesis, Institut fur Kernphysik Johann Wolfgang Goethe Universitat Frankfurt am Main, August 2006. → page 61

[33] A. A. Milner, J. A. M. Fordyce, I. MacPhail-Bartley, W. Wasserman, V. Milner, I. Tutunnikov, and I. S. Averbukh. Controlled enantioselective orientation of chiral molecules with an optical centrifuge. *Phys. Rev. Lett.*, 122, 2019. doi:10.1103/PhysRevLett.122.223201. URL https://link.aps.org/doi/10.1103/PhysRevLett.122.223201. → page 3

[34] J. Oberheide, P. Wilhelms, and M. Zimmer. New results on the absolute ion detection efficiencies of a microchannel plate. *Measurement Science and Technology*, 8:351, 1999. doi:10.1088/0957-0233/8/4/001. → page 47

[35] H. Pauly. *Atom, Molecule, and Cluster Beams I: Basic Theory, Production and Detection of Thermal Energy Beams*, volume 28. Springer Berlin Heidelberg, 2000. doi:10.1007/978-3-662-04213-7. → page 27

[36] D. Pentlehner, J. H. Nielsen, A. Slenczka, K. Mølmer, and H. Stapelfeldt. Impulsive laser induced alignment of molecules dissolved in helium nanodroplets. *Phys. Rev. Lett.*, 110, 2013. doi:10.1103/PhysRevLett.110.093002. URL https://link.aps.org/doi/10.1103/PhysRevLett.110.093002. → page 59

[37] J. D. Pickering, B. Shepperson, L. Christiansen, and H. Stapelfeldt. Alignment of the CS_2 dimer embedded in helium droplets induced by a circularly polarized laser pulse. *arXiv:1901.03184 [physics]*, 2019. → pages 40, 50

[38] E. Polyakova. *Multiphoton Ionization Of Molecules Embedded In Superfluid Liquid Helium Droplets*. PhD thesis, University OF Southern California, 2005. → page 21

[39] K. Schneider. Implementation and characterisation of a new shutter for helium nanodroplet isolation spectroscopy. Master's thesis, University of Freiburg, 2017. → pages 29, 30

[40] B. Shepperson, A. A. Søndergaard, L. Christiansen, J. Kaczmarczyk, R. E. Zillich, M. Lemeshko, and H. Stapelfeldt. Laser-induced rotation of iodine molecules in helium nanodroplets: Revivals and breaking free. *Phys. Rev. Lett.*, 118, 2017. doi:10.1103/PhysRevLett.118.203203. → pages 2, 59

[41] H. Stapelfeldt and T. Seideman. Colloquium: Aligning molecules with strong laser pulses. *Rev. Mod. Phys.*, 75, 2003. doi:10.1103/RevModPhys.75.543. → pages 13, 44

[42] M. Stei, J. von Vangerow, R. Otto, A. Kelkar, E. Carrascosa, T. Best, and R. Wester. High resolution spatial map imaging of a gaseous target. *The Journal of chemical physics*, 138, 06 2013. doi:10.1063/1.4807482. → page 57

[43] F. Stienkemeier and K. Lehmann. Topical review: Spectroscopy and dynamics in helium nanodroplets. *Journal of Physics B-atomic Molecular and Optical Physics - J PHYS-B-AT MOL OPT PHYS*, 39, 04 2006. doi:10.1088/0953-4075/39/8/R01. → page 1

[44] R. Tanyag, C. Jones, C. Bernando, S. O'Connell, D. Verma, and A. Vilesov. *CHAPTER 8: Experiments with Large Superfluid Helium Nanodroplets*. 01 2018. doi:10.1039/9781782626800-00389. → pages ix, 20, 42

[45] A. F. Toennies, J. Peter; Vilesov. Superfluid helium droplets: A uniquely cold nanomatrix for molecules and molecular complexes. *Cheminform*, 35(27), 2004. → pages viii, 1, 21, 40

[46] D. Townsend, M. Minitti, and A. Suits. Direct current slice imaging. *Review of Scientific Instruments*, 74:2530–2539, 2003. doi:10.1063/1.1544053. → page 45

[47] J. Underwood, I. Procino, L. Christiansen, J. Maurer, and H. Stapelfeldt. Velocity map imaging with non-uniform detection: Quantitative molecular axis alignment measurements via coulomb explosion imaging. *The Review of scientific instruments*, 86, 2015. doi:10.1063/1.4922137. → page 45

[48] X. Wang, J. Zhang, S.-A. Zhang, and Z.-R. Sun. Coulomb explosion of CS_2 molecule under an intense femtosecond laser field. *Chinese Physics B*, 25, 2016. doi:10.1088/1674-1056/25/5/053301. → page 47

[49] W. W. Wasserman. Implementation of a mechanical shutter for studying the critical velocity in superfluid helium nanodroplets. Master's thesis, The University of British Columbia, 2018. → page 30

[50] B. J. Whitaker. *Imaging in molecular dynamics : technology and applications : a user's guide*. Cambridge University Press, 2003. → page 68

[51] D. Williams, editor. *Molecular Physics: Methods of Experimental Physics, Part 2*, volume 3. Academic Press, Inc., 2 edition, 1974. → page 19

[52] C. Wu, Y. Yang, Z. Wu, B. Chen, H. Dong, X. Liu, Y. Deng, H. Liu, Y. Liu, and Q. Gong. Coulomb explosion of nitrogen and oxygen molecules through non-Coulombic states. *Physical Chemistry Chemical Physics*, 13, 2011. doi:10.1039/C1CP21345H. → page 47

[53] S. Yang and A. M. Ellis. Helium droplets: a chemistry perspective. *Chemical Society Reviews*, 42(2), 2013. doi:10.1039/C2CS35277J. → page 19

[54] A. Zhao, P. Sándor, and T. Weinacht. Coincidence velocity map imaging using a single detector. *The Journal of Chemical Physics*, 147, 2017. doi:10.1063/1.4981917. → page 51